New Journal of Physics
The open-access journal for physics

$Tl_2Ba_2CuO_{6+\delta}$ brings spectroscopic probes deep into the overdoped regime of the high-T_c cuprates

D C Peets[1], J D F Mottershead[1], B Wu[1], I S Elfimov[1], Ruixing Liang[1], W N Hardy[1], D A Bonn[1], M Raudsepp[2], N J C Ingle[1] and A Damascelli[1]

[1] Department of Physics and Astronomy, University of British Columbia, Vancouver, BC V6T 1Z1, Canada
[2] Department of Earth and Ocean Sciences, University of British Columbia, Vancouver, BC V6T 1Z4, Canada
E-mail: bonn@physics.ubc.ca and damascelli@physics.ubc.ca

New Journal of Physics **9** (2007) 28
Received 5 September 2006
Published 14 February 2007
Online at http://www.njp.org/
doi:10.1088/1367-2630/9/2/028

Abstract. Single-particle spectroscopic probes, such as scanning tunnelling and angle-resolved photoemission spectroscopy (ARPES), have provided us with crucial insights into the complex electronic structure of the high-T_c cuprates, in particular for the under- and optimally-doped regimes where high-quality crystals suitable for surface-sensitive experiments are available. Conversely, the elementary excitations on the heavily overdoped side of the phase diagram remain largely unexplored. Important breakthroughs could come from the study of $Tl_2Ba_2CuO_{6+\delta}$ (Tl2201), a structurally simple system whose doping level can be tuned from optimal to extreme overdoping by varying the oxygen content. Using a self-flux method and encapsulation, we have grown single crystals of Tl2201, which were then carefully annealed under controlled oxygen partial pressures. Their high quality and homogeneity are demonstrated by narrow rocking curves and superconducting transition widths. For higher dopings, the crystals are orthorhombic, a lattice distortion stabilized by O interstitials in the TlO layer. These crystals have enabled the first successful ARPES study of both normal and superconducting-state electronic structure in Tl2201, allowing a direct comparison with the Fermi surface from magnetoresistance and the gap from thermal conductivity experiments. This establishes Tl2201 as the first high-T_c cuprate for which a surface-sensitive single-particle spectroscopy and a comparable bulk transport technique have arrived at quantitative agreement on a

PII: S1367-2630(07)32075-2
© IOP Publishing Ltd and Deutsche Physikalische Gesellschaft

major feature such as the normal state Fermi surface. The momentum dependence of the ARPES lineshape reveals, however, an unexpected phenomenology: in contrast to the case of under- and optimally-doped cuprates, quasiparticles are sharp near $(\pi, 0)$, the antinodal region where the gap is maximum, and broad at $(\pi/2, \pi/2)$, the nodal region where the gap vanishes. This reversed quasiparticle anisotropy past optimal doping, and its relevance to scattering, many-body, and quantum-critical phenomena in the high-T_c cuprates, is discussed.

Contents

1. Introduction **2**
2. Tl2201 single-crystal preparation **6**
2.1. Single-crystal growth 7
2.2. Physical and chemical analysis 8
2.3. Structural analysis: crystallinity and symmetry 9
3. The low-energy electronic structure of Tl2201 **11**
3.1. Band structure calculations 12
3.2. Electronic dispersion and Fermi surface by ARPES 14
3.3. ARPES study of the superconducting gap. 17
3.4. ARPES lineshape analysis. 20
4. Discussion and conclusions **25**
Acknowledgments **28**
References **28**

1. Introduction

The cuprate superconductors can be tuned through a remarkable progression of states of matter by doping charge carriers into the CuO_2 planes [1, 2]. The most generic feature of this tuning is a sequence from an antiferromagnetic insulator, through a doping range where the superconducting critical temperature builds to a maximum (optimal doping) and then dies away again at higher doping, in the so-called overdoped regime (figure 1). This sequence contains three separate touchstones for an understanding of the cuprates: the Mott insulator, which is known to result from very strong electron–electron repulsion and is antiferromagnetically ordered, the d-wave superconductor, and the overdoped metal. The latter is widely believed to exhibit less exotic normal-state properties and might be understood through Fermi liquid theory. Over the last two decades, a great deal of experimental work has been done on undoped, underdoped, and optimally doped cuprates, aiming at elucidating the connection between the antiferromagnetic insulator and high-T_c superconductor (HTSC), and the role of electronic correlations in the emergence of superconductivity. However, the testing of Fermi liquid theory in the overdoped regime has been severely hampered by a lack of compounds that can actually be doped to this high level and, at the same time, are suitable for a wide range of experimental techniques.

In the struggle to understand high-T_c superconductivity, the quest for better materials to study remains key. Researchers want samples that can be grown very cleanly, can be doped

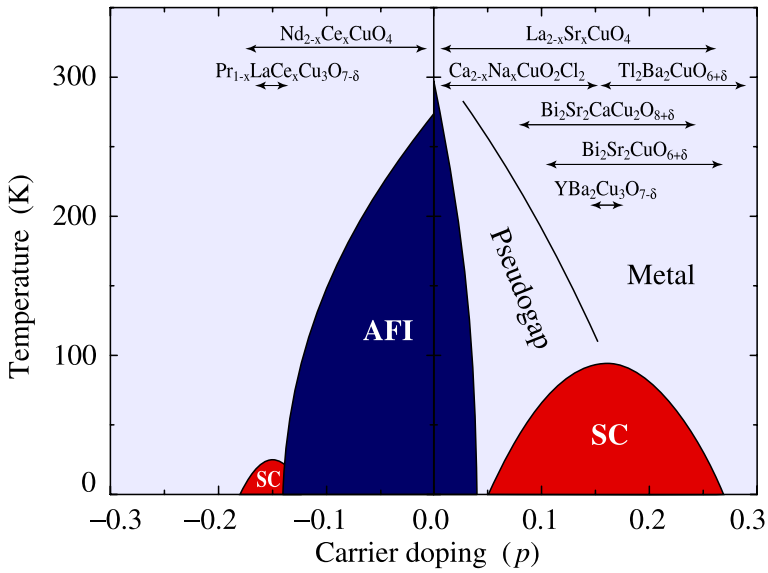

Figure 1. Temperature-doping phase diagram for electron ($p < 0$) and hole-doped ($p > 0$) cuprates. The doping range explored by ARPES for those materials more extensively studied is indicated by the corresponding arrows.

over a very wide range of the phase diagram, and are suitable for a variety of bulk and surface measurements. Surface-sensitive techniques in particular, such as angle-resolved photoemission spectroscopy (ARPES) [3, 4] and scanning tunnelling microscopy (STM) and scanning tunnelling spectroscopy (STS) [5], introduce additional constraints with regard to sample requirements. These highly sophisticated spectroscopic probes can be used to obtain information on the single-particle excitation spectrum of a solid—i.e. the spectral function $A(\mathbf{k}, \omega)$ that can be calculated in terms of the electron Green's function starting from the microscopic many-body Hamiltonian of the system [6]—but only if the material can be cleaved to expose a well-defined and stable surface (i.e. which does not reconstruct into a form that obscures the bulk electronic structure).

A summary of the approximate doping range explored by ARPES on different HTSC families is given in figure 1. On the undoped side of the phase diagram ($p = 0$), the parent compounds $Ca_2CuO_2Cl_2$ and $Sr_2CuO_2Cl_2$ yield excellent cleaved [001] faces. These have allowed ARPES studies of the electronic structure of the correlated antiferromagnetic insulator and of the magneto-elastic interactions associated with the propagation of a single hole in the two-dimensional (2D) spin background [3]. Via hole doping, one can drive these materials through a metal-insulator transition and enter the superconducting dome (in this paper, we will focus on the hole-doped side of the phase diagram, $p > 0$). For instance, recent STM, STS [7], and ARPES [8] experiments on the underdoped superconductor $Ca_{2-x}Na_xCuO_2Cl_2$ have suggested the existence of new electronic ordering phenomena in the doping region between the insulator and the superconductor, possibly in the form of glassy electronic behaviour or a surface-nucleated phase transition since more conventional long-range charge order was not observed in scattering studies [9]. Near optimal doping, where the cuprates exhibit their highest superconducting critical temperatures, $YBa_2Cu_3O_{7-\delta}$ stands out as the cleanest material and has been used extensively in bulk-sensitive studies of the normal and superconducting properties, such as the symmetry of the order parameter [10]–[12], superfluid density [13], charge and thermal transport [14], low-energy

electrodynamics [15, 16], vibrational and magnetic excitation spectra [17, 18]. Unfortunately, this material is complicated by the presence of CuO-chain layers and does not have a neutral [001] cleavage plane for surface-sensitive techniques. In particular, $YBa_2Cu_3O_{7-\delta}$ cleaves between the chain layer and the BaO layer. BaO surfaces have had the nearest source of dopants (the CuO chains) removed, so that their hole-doping is uncertain. STS shows that the CuO chain surfaces are characterized by prominent surface density waves [19] and differ substantially from the bulk. They exhibit surface states, as seen in ARPES [20], and possess unavoidable doping disorder. These problems have severely limited the availability of single-particle spectroscopy data from ARPES [21, 22], STM, and STS [19, 23].

Extensive ARPES investigations have been performed on $La_{2-x}Sr_xCuO_4$ [3, 24], over a broad doping range extending from the undoped insulator ($x = 0$) to the overdoped superconductor ($x = 0.22$; note that $x = p$ for this compound). This system, however, is affected by severe cation disorder associated with La–Sr substitution right next to the CuO_2 plane, as well as lattice, charge, and magnetic instabilities, which might provide an explanation for why the maximum T_c in this compound is suppressed with respect to other single-layer materials [25]. In turn, many of the key bulk-sensitive measurements requiring perfect crystals and long mean free paths could not be performed on this material family. In addition, neither STM nor STS experiments have been successful so far on cleaved $La_{2-x}Sr_xCuO_4$, probably because both the CuO_2 and $La_{1-\frac{x}{2}}Sr_{\frac{x}{2}}O$ surfaces are polar, with a charge $Z_{CuO_2} = -(2-x)$ and $Z_{(La,Sr)O} = (1 - x/2)$, and thus critically unstable. To date, the most rich spectroscopic information on high-T_c cuprates from both STS and ARPES have been obtained on the Bi compounds, in particular $Bi_2Sr_2CuO_{6+\delta}$ and $Bi_2Sr_2CaCu_2O_{8+\delta}$ [3]–[5]. However, similar to $La_{2-x}Sr_xCuO_4$, this family has greater problems with disorder than $YBa_2Cu_3O_{7-\delta}$ [25], leaving a disconnection between materials for which we have the most information. This dilemma interferes with strict tests of the theory of high-T_c superconductivity, in which one must connect the single particle excitations to the other physical properties and dynamic susceptibilities [26].

A further problem in the study of HTSCs is that, due to the high T_c values, the physical properties of the underlying normal state can be probed only at relatively high temperatures. This often makes the detailed interpretation of the experimental results more complex and less informative (e.g. charge and thermal conductivity, Hall number, magnetoresistance, etc), or can even make some experiments completely unfeasible (as in the case of the de Haas–van Alphen effect). Alternatively, at least for certain techniques, one can access the low-temperature normal-state properties by suppressing superconductivity via the application of an external magnetic field. Once again however, due to the very high T_c and in turn the extraordinarily large value of the second critical field H_{c2}, this approach is precluded near optimal doping for the cleanest cuprates. Extreme overdoping is a means of reducing both T_c and H_{c2}, so that one can study both the superconducting and underlying normal states, but here most samples tend to be less clean because of the need to dope with large concentrations of cation impurities, such as Sr in La_2CuO_4 and Pb in $Bi_2Sr_2CuO_{6+\delta}$ [25]. In this case it can be unclear whether changes observed in the material's properties are attributable to the increased doping, or the increased scattering or other extrinsic effects. Due to these material and experimental limitations, the underlying normal state of HTSCs, the heavily overdoped side of the phase diagram, and the metallic state that emerges beyond the end of the superconducting dome have remained largely unexplored.

The most promising compound for investigating the deeply overdoped regime is the single-layer system $Tl_2Ba_2CuO_{6+\delta}$ (Tl2201, see figure 2), whose natural doping range varies from optimal to extreme overdoping as one increases the oxygen content δ. Tl2201 has two extremely

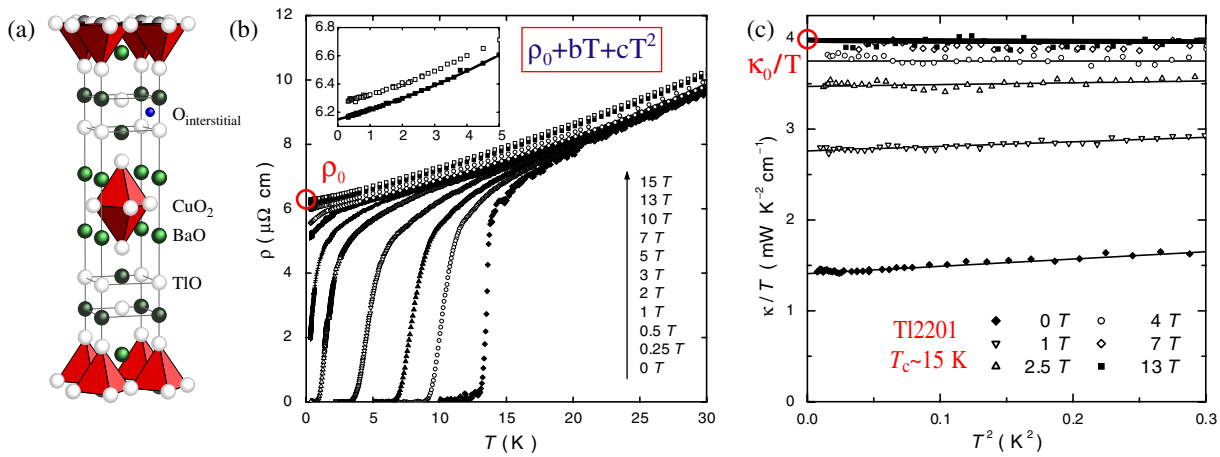

Figure 2. (a) Unit cell of Tl2201; the position of interstitial oxygen in the Tl_2O_2 bilayer is also shown. (b, c) Electrical resistivity and thermal conductivity of overdoped Tl2201 ($T_c \simeq 15$ K), plotted versus temperature for different values of an external magnetic field applied normal to the CuO_2 planes (after [27]). From the $T = 0$ K intercepts of $\rho(T)$ and $\kappa(T)/T$, the ratio $\rho_0\kappa_0/T = 0.99 \pm 0.01 L_0$ was calculated ($L_0 = 2.44 \times 10^{-8}$ W Ω K^{-2} is Sommerfeld's value for the Lorenz ratio $L \equiv \kappa/\sigma T$). This indicates that the Wiedemann–Franz law is obeyed in overdoped cuprates although the normal-state $\rho(T)$ is dominated by a non Fermi-liquid like T-linear term (see inset of panel (a)).

flat CuO_2 planes located far apart from each other in the body-centred unit cell; there are no complicating chain layers (as in the Y-based cuprates), or bilayer band-splitting effects (as in $Bi_2Sr_2CaCu_2O_{8+\delta}$ and $YBa_2Cu_3O_{7-\delta}$). Like La and Bi-based systems, Tl2201 can exhibit a cation non-stoichiometry but this consists of Cu substituting Tl in the Tl_2O_2 double layer, thus farther removed from the CuO_2 planes than the Bi–Sr or La–Sr substitutions that have been shown to have a large impact on the superconductivity of the Bi and La cuprates [25]. Tl2201 may be reversibly doped through interstitial oxygen and, near optimal doping, vacancies in the Tl_2O_2 bilayer [28]. The ability to overdope a crystal reversibly from optimal doping to the full suppression of superconductivity, by changing its oxygen content alone, is a fortuitous property of Tl2201, although this has been successfully demonstrated over the whole doping range only on ceramic samples.

A variety of bulk properties have already been studied in Tl2201. At optimal doping, the pure $d_{x^2-y^2}$ symmetry of the superconducting gap was confirmed by phase-sensitive measurements [29], and the so-called magnetic resonant mode at 47.5 meV was detected below T_c in neutron scattering experiments [30], the first time for a single-layer cuprate. The high sample quality has been recently demonstrated by measurements of angular magnetoresistance oscillations (AMRO), a bulk transport technique that requires the long mean free paths afforded by high purity and crystallinity [31]. The AMRO study of Tl2201 resulted in the first estimate of the normal state Fermi surface of a cuprate superconductor from a bulk sensitive probe. The combination of charge [27, 32] and heat [27] transport measured at low temperature on very overdoped Tl2201 in the normal state, by applying up to 13T magnetic fields to suppress superconductivity (see figure 2), allowed the Lorenz ratio $L \equiv \kappa/\sigma T$ to be extracted. The value obtained, $0.99 \pm 0.01\, L_0$

(where $L_0 = 2.44 \times 10^{-8}\,\mathrm{W\,\Omega\,K^{-2}}$ is Sommerfeld's value), lead to the conclusion that the Wiedemann–Franz law is obeyed in overdoped cuprates [27]: the electronic carriers of heat are fermionic excitations of charge $-e$, suggesting that the low-energy excitations in overdoped cuprates might indeed be described in terms of Fermi-liquid quasiparticles. At variance with the hints of Fermi-liquid-like behaviour, however, the *ab*-plane resistivity is not purely described by a T^2 power law but is still dominated by a T-linear term (see inset of figure 2). In this context, the detailed study of Tl2201 with modern single particle spectroscopies would be extremely desirable, as it might provide direct insights into the nature of the quasiparticles (QPs) in both the normal and superconducting states [3, 4, 6].

Unfortunately, despite its great potential, progress on the Tl2201 system has been slow because of difficulties in the growth of single crystals. Thallium oxide is volatile, reactive, and highly toxic, a combination which places stringent constraints on crystal growth techniques. Standard procedures such as flux-growth in open crucibles or the use of a floating zone image furnace would allow toxic vapours to escape into the lab and deplete the thallium in the reaction vessel by allowing it to sublime out in a colder part of the furnace. It is thus essential to contain the growth components within a non-reactive enclosure so that thallium is not lost through either reaction or evaporation. In section 2, we report on our effort in the growth of high-purity single crystals of Tl2201, by a copper-rich self-flux method, and in their careful annealing in a controlled oxygen atmosphere. These samples can be cleaved to expose a clean and stable [001] surface suitable for single particle spectroscopy experiments, as was demonstrated by our first successful study of the Fermi surface and QP excitations of Tl2201 by ARPES [33]. The comprehensive ARPES investigation of several doping levels will be presented in section 3, and a discussion linked to other theoretical and experimental results will be given in section 4. The quantitative agreement between the ARPES and AMRO [31] determined Fermi surfaces indicates that Tl2201 may be a suitable testing ground for finally joining together the modern single particle spectroscopies and a host of well-established bulk probes of metals and superconductors. In particular, Tl2201 might be the ideal cuprate for a broad-based study of the normal metal that may underlie the superconductor in the overdoped regime, providing an understandable anchor point in the phase diagram of the high-temperature superconductors.

2. Tl2201 single-crystal preparation

Difficult to prepare even as a ceramic, Tl2201 is even more challenging to grow as a crystal. Tl2201 melts incongruently and its crystals are grown from a high temperature non-stoichiometric melt made of the Tl2201 components. Ideally, this melt would be decanted to reveal freestanding flux-free crystals. While this technique is in common use for the growth of complex oxide crystals, there are a few challenges particular to Tl2201 system. The difficulties are due to the thallium oxide precursor. Around 800 °C, trivalent thallium oxide decomposes into a monovalent oxide and oxygen gas [34]

$$\mathrm{Tl_2O_3} \rightleftharpoons \mathrm{Tl_2O} + \mathrm{O_2}\uparrow .$$

While the oxygen gas evolved must be allowed to escape, this decomposition leads to a more serious problem: at growth temperatures, the monovalent oxide's vapour pressure is of the order of 0.1 atm, high enough to allow it to escape rapidly. If the $\mathrm{Tl_2O}$ gas leaves the crucible, however slowly, the composition of the melt will be at best time-varying and at worst quickly devoid of

thallium. The volatility of Tl_2O can also make the subsequent annealing of the crystals difficult, as the crystal surface may slowly decompose at temperatures at which the oxygen atoms are mobile. There are several procedures that may be employed to mitigate these problems, including using pre-reduced thallium precursors such as $Tl_2Ba_2O_5$ [35], encapsulation [36], or very high oxygen partial pressures. A further issue is that Tl_2O is quite reactive, most notably reacting with the quartz often used for encapsulation and furnace tubes.

To date, only a handful of groups have grown crystals of Tl2201. Mackenzie's group, using a gold lid on their crucible as a barrier to diffusion, found they could only successfully obtain crystals within a 2 °C by 2 min window [37, 38]. Hasegawa *et al* used reduced thallium precursors and an alumina high-pressure bomb to control thallium loss [36, 39]. Kolesnikov *et al* [40]–[42] do not report any special precautions for controlling the loss of thallium. In our growth effort (see subsection 2.1), we developed a flexible sealing scheme that permits the oxygen to escape as it is evolved, while at the same time containing the Tl_2O.

A last crucial issue with the preparation of Tl2201 single crystals, alluded to above, is that the crystal surfaces can degrade during the oxygen post-annealing required to set the charge carrier content and, in turn, the temperature of the superconducting phase transition. So far most work on annealing of Tl2201 has been carried out on ceramic samples [43], but annealing of single crystals, where surface damage is more obvious, has been less successful—only Mackenzie's group reported success [37]. As a result, many crystals studied to date have been unannealed, resulting in inhomogeneous oxygen content and broad transitions ($\Delta T_c = 10$–20 K), which can obscure many features and add unnecessary disorder. As part of our growth effort, we have also carefully explored the annealing of Tl2201 single crystals, succeeding in the preparation of samples ranging from near optimal doping to very overdoped, while avoiding surface damage.

2.1. Single-crystal growth

For the crystal growth, we employ a copper-rich self-flux technique using a barium and copper precursor, $BaCuO_2$. It was prepared in powder form from 99.999% pure $BaCO_3$ and 99.995% pure CuO by repeated calcining under flowing oxygen. The use of carbonate-free barium cuprate avoids both carbon poisoning from $BaCO_3$ and the cation impurities that may be encountered if one employs BaO_2, which is only available at lower cation purity. Carbon contamination is of particular concern in this system because there are several known superconducting thallium-based oxycarbonates [44].

The barium cuprate powder was mixed with 99.99% pure Tl_2O_3 to a final cation ratio of Tl : Ba : Cu = 1.05 : 1 : 1 [45], then loaded into a 10 ml alumina crucible. The crucible was sealed using a gold lid fixed in place with a 1 kg weight. Employing this sealing scheme, O_2 gas may still escape as Tl_2O_3 decomposes, but the seal becomes very effective once the contents of the crucible equilibrate at the growth temperature, thus preventing significant loss of Tl_2O (as monitored by mass-loss measurements). The charge was heated rapidly (300° C h^{-1}) to 935 °C, while flowing oxygen to flush out any escaping thallium oxide, and held for 12 h to equilibrate. It was cooled at -0.5 °C h^{-1} to 890 °C, then allowed to cool freely to room temperature. The oxygen gas flowing through the furnace was bubbled through sulphuric acid and water to remove any escaped thallium that did not condense in colder areas of the furnace. Most resulting crystals were embedded in flux, but free-standing platelet single crystals of 1–2 mm^2 were harvested from voids in the flux ingot. As shown in figure 3(a), these crystals exhibited mirror surfaces with fine,

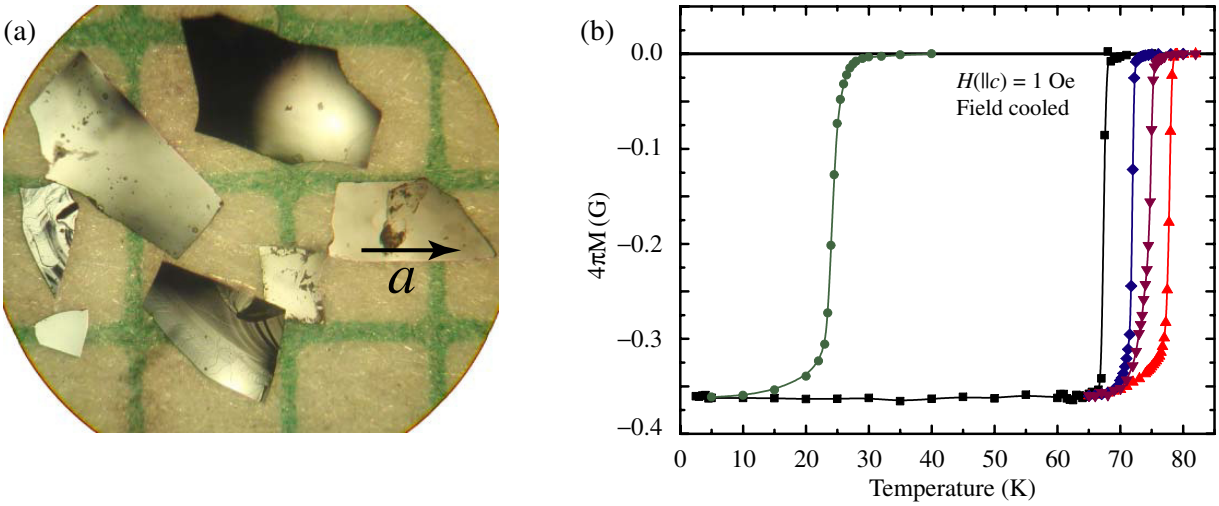

Figure 3. (a) Photo of several Tl2201 crystals on millimetre graph paper; the orthorhombic *a*-axis of one crystal is marked. (b) Field-cooled magnetization curves for Tl2201 crystals annealed to different hole-doping levels; the sharpness of the superconducting transitions is an indication of the crystals' homogeneity.

curved growth steps. All characterization and spectroscopy reported here were performed on flux-free, void-grown single crystals.

The as-grown samples typically have superconducting transitions of 5–10 K (onset) and several Kelvins wide, a width comparable to other groups' as-grown samples. As-grown T_cs are determined by the cation substitution level, crystal dimensions, cooling rate, and the atmosphere around the crystals, the last two parameters being coupled through the equation of state for oxygen gas. The broad superconducting transition of as-grown crystals is mainly due to variations of the doping throughout the crystal and it is crucial that the crystals be annealed before they are studied. The crystals were annealed under controlled oxygen partial pressures at temperatures between 290 °C and 500 °C. This produces samples whose oxygen contents place them on the overdoped side of the phase diagram, with sharp superconducting transitions ranging from 5 to 85 K. We have not attempted to reach optimal doping, which in this system is believed to correspond to a superconducting T_c of at least 93 K [28], because even higher annealing temperatures are required, which increases the risk of thallium loss.

2.2. Physical and chemical analysis

Since cation substitution can cause increased scattering, one objective of this study was to grow crystals with the lowest possible cation substitution level. Of more immediate importance than the reduction of cation defects, however, is reproducibility. Because cation substitution also dopes the crystal, variation between crystals would lead to different T_cs as well as different scattering rates. More problematic still would be a variation within a crystal, which could arise from changes in the composition of the melt over the course of the crystal's growth. Although cation substitution is not desired and does dope the crystals, it must be emphasized that this is not used as a control parameter in doping these crystals. If the crystals can be grown with a reproducible level of cation substitution, the cation disorder will be the same for all dopings.

This is in contrast to LSCO, where cation substitution is the primary control parameter, and must be varied by roughly a factor of four to traverse the superconducting dome.

To determine the levels of cation substitution in our crystals, electron-probe micro-analyses (EPMA) of several crystals were performed on a fully-automated CAMECA SX-50 instrument in wavelength-dispersion mode.[3] The cation composition (normalized to the barium content) was determined to be $Tl_{1.884(6)}Ba_2Cu_{1.11(1)}O_{6+\delta}$ and was not observed to be position dependent on individual crystals, nor did it vary between crystals. This result corresponds to a level of copper substitution at the thallium site comparable to that reported previously [37, 38, 42, 47] for cation-substituted Tl2201. Al contamination was checked separately by EPMA and found to be below the 50 ppm detection limit, corroborating our observation that the crucibles were not corroded by the melt.[4] Despite the cation non-stoichiometry, the high quality of these crystals is evidenced by their narrow superconducting transitions, measured by magnetization in a Quantum Design SQUID magnetometer (MPMS). figure 3(b) shows the field-cooled magnetization measured at 1 Oe ($H \parallel c$), for crystals with transition widths (10–90%) ranging from 4 to 0.7 K. The observed 40–60% Meissner fraction (i.e., fraction of flux excluded when cooling through T_c) compares well with field-cooled results on other superconducting cuprates. Note that Tl2201's extremely low first critical field (H_{c1}) makes the transitions appear broader in higher fields.

2.3. Structural analysis: crystallinity and symmetry

To investigate the samples' crystallinity, x-ray diffraction spectra and rocking curves were taken on a BEDE model 200 double-crystal diffractometer with a Si(111) monochromator; the entire sample was illuminated by the x-ray beam. Figure 4(a) depicts the (0 0 10) x-ray rocking curve of a $0.5 \times 1.2\,\mathrm{mm}^2$ crystal annealed to $T_c = 67.7$ K. While the FWHM of 0.034° is broader than the 0.006° obtained for the best $YBa_2Cu_3O_{7-\delta}$ crystals grown in $BaZrO_3$ crucibles, it is similar to the 0.02–0.03° achieved for $YBa_2Cu_3O_{7-\delta}$ grown in YSZ crucibles [48], indicating a good degree of crystalline perfection. A crystal annealed to achieve a relatively high oxygen content and strong overdoping ($T_c = 24$ K) was found to be orthorhombic with lattice parameters $a = 5.4580(3)$ Å, $b = 5.4848(5)$ Å and $c = 23.2014(5)$ Å, consistent with the lattice constants reported for ceramics with similar T_c and Cu substitution [28]. This orthorhombicity is determined from the x-ray diffraction data presented in figure 4(b): the two data sets were recorded independently for a- and b-axes and would be identical to one another if the crystals were tetragonal. Closer to optimal doping (i.e. at a lower interstitial oxygen content), the $T_c = 67.7$ K sample was tetragonal to within our resolution.

[3] The EPMA was performed under the following operating conditions: excitation voltage, 15 kV; beam current, 20 nA; peak count time, 80 s; background count time, 40 s; and spot diameter, 10 μm. Data reduction was performed using the 'PAP' $\varphi(\rho Z)$ method [46]. For the elements studied, the following standards, x-ray lines and monochromator crystals were used: elemental Tl, Tl$M\alpha$, PET; $YBa_2Cu_3O_{6.920}$, Ba$L\alpha$, PET; and $YBa_2Cu_3O_{6.920}$, Cu$K\alpha$, LIF. Tight pulse height analysis (PHA) control was used to eliminate to the degree possible any interference from higher-order lines.

[4] Operating conditions were the following: excitation voltage, 15 kV; beam current, 40 nA; peak count time, 500 s; background count time, 250 s; and spot diameter, 10 μm. The matrix composition was fixed at stoichiometric; Al$K\alpha$ was standardized on α-Al_2O_3 using a TAP crystal monochromator.

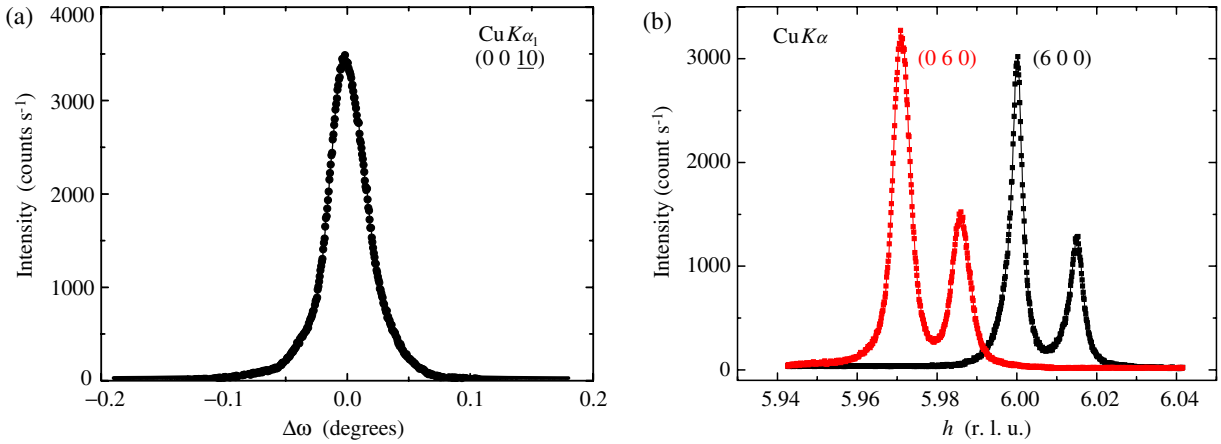

Figure 4. (a) The (0 0 10) rocking curve for a typical Tl2201 single crystal $T_c = 67.7$ K); the FWHM is 0.034°, indicating excellent crystallinity. (b) The (6 0 0) and (0 6 0) peaks for a $T_c = 24$ K sample, showing the orthorhombicity (the doublets result from the presence of both Cu$K\alpha_1$ and Cu$K\alpha_2$ radiation).

Tl2201's crystal symmetry depends on the level of cation substitution and the oxygen content. Stoichiometric and near-stoichiometric ceramics have been shown to be orthorhombic for all oxygen contents, while heavily-substituted ones are strictly tetragonal [49]. For intermediate levels of substitution, the orthorhombicity depends on the oxygen content: samples with higher oxygen contents are more orthorhombic [28]. The orthorhombic distortion is thought to arise from a lattice mismatch between the CuO_2 layer and the naturally larger Tl_2O_2 double layer. Interstitial oxygens, which are believed to be located between two adjacent TlO planes on a unit cell face as in figure 2(a) [28, 50], increase the distortion; cation disorder, instead, seems to suppress it. The distortion and its dependence on the oxygen content δ and the copper substitution y are shown schematically in figure 5. Powder x-ray diffraction shows that the orthorhombic distortion is an elongation along one plaquette diagonal, with the Cu–O bonds remaining the same in both directions. The distortion is quite minor: instead of being at right angles, the Cu–O bonds meet at ≈89.7° in orthorhombic samples. The plaquette diagonals, identified with nodes in the superconducting gap, remain orthogonal, so no mixing of order parameter symmetries is required. For these reasons and for ease of comparison with other systems, all ARPES analysis reported here is based on the original tetragonal unit cell, regardless of the actual symmetry of the crystals.

Our crystals' orthorhombicity, defined as $2(b-a)/(b+a)$, is consistent with that found by Wagner *et al* [28] for similar levels of cation substitution, as shown in figure 6(a). One should keep in mind, however, that this quantity is highly prone to uncertainties because of the smallness of the orthorhombic distortion, so that quantitative conclusions based on this graph should be treated with caution. Figure 6(b) compares two of our annealed crystals' c-axis lattice parameters to the orthorhombic ceramic samples of Wagner *et al* [28] and Shimakawa *et al* [49]. Our c-axis lattice parameters are again similar to those of Wagner *et al* [28], but we observe higher T_c values for the same lattice parameters (or a shorter c-axis for the same T_c). Possible explanations for this include improvements in T_c from higher homogeneity, cleaner samples or larger grain size (crystals versus ceramics), more homogeneous annealing, or possibly a calibration disagreement

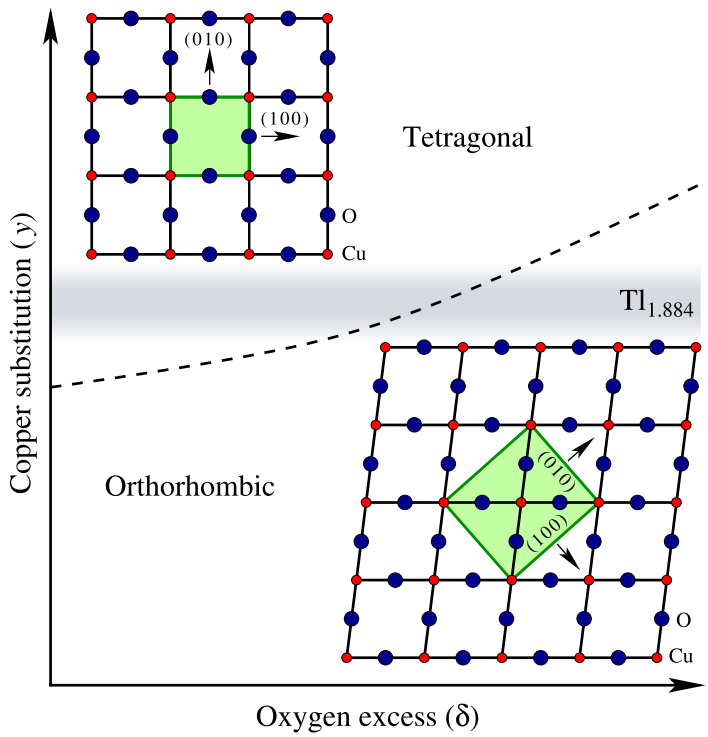

Figure 5. Schematic depiction of the dependence of the orthorhombic/tetragonal structural transition on y and δ in $Tl_{2-y}Ba_2Cu_{1+y}O_{6+\delta}$. This scenario is suggested by the data from polycrystalline samples of Wagner *et al* [28] and our own single crystal diffraction results (see figure 6). The CuO_2 plane and unit cell (in green) are shown with and without the orthorhombic distortion, which is here exaggerated for clarity. The grey bar indicates where our crystals fall on this plot: $y = 0.116$.

between the diffractometers. Wagner's samples have transitions a few Kelvins wide, with long tails towards zero Kelvin; also, T_c was defined using the 50% point, which may not be an accurate average of the bulk in such a situation.

3. The low-energy electronic structure of Tl2201

ARPES is an important tool in the study of the electron dynamics in correlated-electron systems. Within the sudden approximation, it probes the energy and momentum dependence of the electronic excitation spectrum of an $N-1$ particle system, the so-called electron-removal portion of the single-particle spectral function $A(\mathbf{k}, \omega)$ [6]. In the non-interacting picture, this spectral function consists of delta-function peaks located at the precise energy and momentum given by the band structure, i.e. $A(\mathbf{k}, \omega) = \delta(\omega - \epsilon_{\mathbf{k}})$. When interactions are considered, the single-particle spectral function is modified by the inclusion of the electron proper self energy $\Sigma(\mathbf{k}, \omega) = \Sigma'(\mathbf{k}, \omega) + \mathrm{i}\Sigma''(\mathbf{k}, \omega)$, which captures all of the many-body correlation effects. One can then write $A(\mathbf{k}, \omega) = -\frac{1}{\pi}(\Sigma''(\mathbf{k}, \omega)/[\omega - \epsilon_{\mathbf{k}} - \Sigma'(\mathbf{k}, \omega)]^2 + [\Sigma''(\mathbf{k}, \omega)]^2)$. With

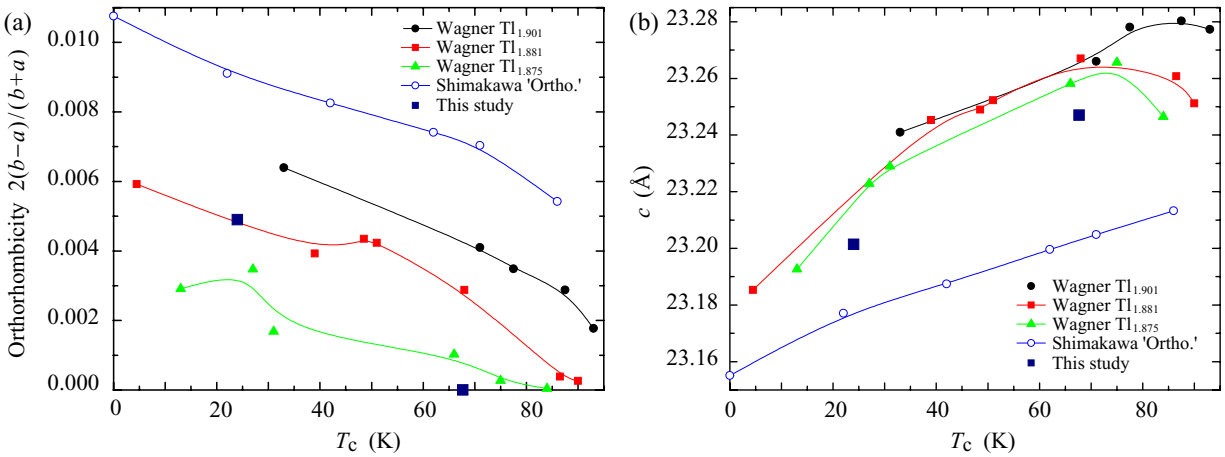

Figure 6. Comparison of our T12201 single crystals with Wagner's [28] and Shimakawa's [49] ceramic samples: (a) orthorhombicity and (b) c-axis lattice constant plotted versus T_c.

respect to the non-interacting case, the peaks in the spectral function shift in energy and gain a finite width, in a way dependent on the energy and momentum of the excitations. At those ω and k for which the spectral function is still characterized by a single pole, energy and lifetime renormalization are directly described by $\Sigma'(\mathbf{k}, \omega)$ and $\Sigma''(\mathbf{k}, \omega)$, respectively. The ARPES lineshape thus gives direct access to the lifetime of the excitation and can provide insights into the nature of the underlying interactions, for example whether or not electron–electron interactions are Fermi liquid-like, as mentioned in relation to the Tl2201 transport data of figure 2. As it will be discussed in the following, the first successful ARPES experiments on Tl2201 [33] have arrived at an agreement with bulk probes on key features such as the normal-state Fermi surface [31] and the superconducting gap [51]. This success suggests that detailed ARPES studies of Tl2201 have the potential to reveal the nature and strength of many-body correlations, upon approaching high-T_c superconductivity from the more conventional overdoped regime.

3.1. Band structure calculations

Since it is generally believed that the normal metal on the very overdoped side of the HTSC phase diagram can be described as a rather conventional Fermi liquid system, in contrast to the strongly correlated Mott insulator found at half filling ($p = 0$ in figure 1), exploring the electronic structure and Fermi surface of heavily overdoped Tl2201 can start with the results of non-interacting band structure calculations performed within the local density approximation (LDA). As shown in figure 2 and especially figure 5, the most important structural element is the CuO_2 planes, which in Tl2201 are well separated from each other by the TlO and BaO layers. As in all cuprates, the CuO_2-derived bands are expected to be the lowest energy states and thus directly determine the macroscopic electronic properties, such as superconductivity.

The results of band structure calculations along the high symmetry directions in the body-centred tetragonal Brillouin zone of Tl2201 are presented in figure 7(a). The electronic structure of undoped (i.e. $\delta = 0$) $Tl_2Ba_2CuO_6$ was calculated using the Stuttgart TBLMTO-47 computer

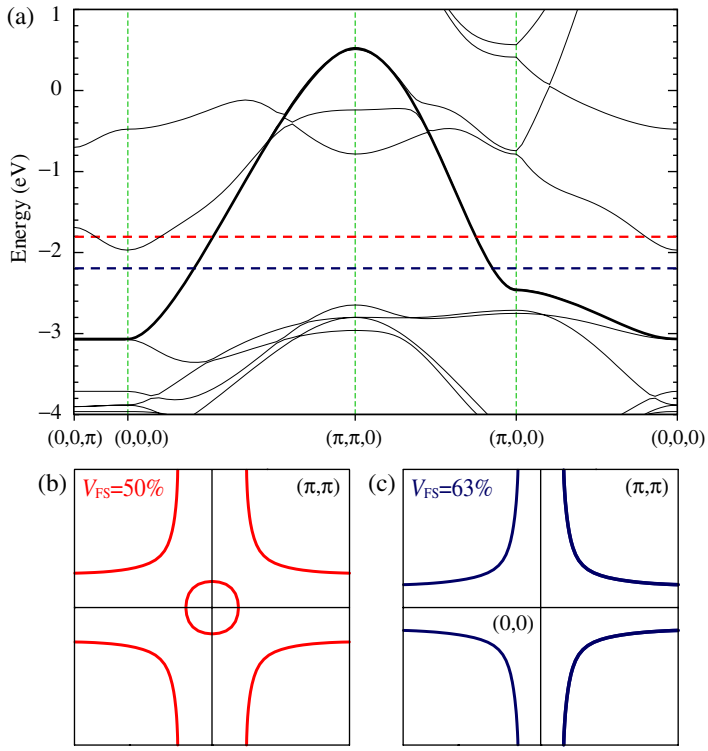

Figure 7. (a) Electronic dispersion obtained from band structure calculations within the LDA. (b, c) Fermi surface calculated for two different doping levels enclosing a volume, counting holes, of 50% (red) and 63% (blue) of the 2D projected Brillouin zone; the corresponding position of the chemical potential with respect to the dispersive electronic bands is indicated in panel (a). Here, as in the rest of the paper, k-space labels are expressed modulo the lattice constants.

code [52]. We used a basis set comprised of 4s, 4p, and 3d orbitals for Cu, of 6s, 6p, 5d, and 4f orbitals for Ba, of 6s, 6p, 5d, and 5f orbitals for Tl, and of 3s and 2p orbitals for oxygen (1s and 2p were used for empty spheres). Coordinates for the atoms are taken from [53]. The essential low-energy feature of the band structure is indeed the highly dispersive Cu($3d_{x^2-y^2}$)–O(1)($2p_{x,y}$) band (bold black line in figure 7(a)); note however that this band is highly 2D, with little dispersion along the k_z direction $(0, 0, k_z = 0) \rightarrow (0, 0, k_z = \pi)$. Its top and bottom are located at (π, π) and $(0, 0)$, respectively, within the 2D projected Brillouin zone; at $(\pi, 0)$ we find the so-called 'extended van Hove singularity', a saddle point in the electronic dispersion which experimentally exhibits a flat dispersion over a much larger momentum region than in the calculations [3]. The other two bands that sit at a comparable energy, i.e. 0 to −2 eV in figure 7(a), are the anti-bonding Tl(6s)–O(2),O(3)(p_z) bands, which do show significant dispersion in the k_z direction. Based on the formal valences of stoichiometric and undoped $Tl_2Ba_2CuO_{6+\delta}$ (2 : 2 : 1 : 6 with Tl^{3+}, Ba^{2+}, Cu^{2+}, O^{2-}; $\delta = 0$), the Fermi energy would be located at the red line in figure 7(a), and both the CuO and TlO bands would cross E_F. This would result in a Fermi surface with hole pockets associated with the CuO band, and a small, spheroidal TlO electron pocket at the $\Gamma = (0, 0, 0)$ point, as in figure 7(b). The presence of this small electron pocket, and the corresponding transfer of electrons from the CuO to the TlO band, were originally proposed as a

possible explanation for why undoped $Tl_2Ba_2CuO_6$ does not show the Mott insulating behaviour typically seen in undoped cuprates, such as La_2CuO_4, which results from the presence of a truly half-filled $3d_{x^2-y^2}$ CuO band [53]. One should also realize that the non-stoichiometry of our samples ($Tl_{1.884(6)}Ba_2Cu_{1.11(1)}O_{6+\delta}$, see subsection 2.2) provides additional hole doping even in the nominally undoped $\delta = 0$ case (~ 0.113 holes/formula unit, from the average between Tl and Cu non-stoichiometry). The latter would push the CuO band further away from half-filling and eventually drive the TlO band above E_F. This shift of the chemical potential would generate a Fermi surface consisting solely of a CuO hole pocket around (π, π) similar to the results shown in blue in figures 7(a) and (c), which were calculated to match the 63% volume observed by ARPES on our $T_c = 30$ K overdoped Tl2201 crystal [33]. Note that if the effect of hole doping through interstitial oxygen were explicitly included in the calculations, the TlO bands would be pushed to much higher energies, beyond the rigid band picture [54]. The analogous effects of Pb substitution or excess oxygen in the Bi–O layers of Bi-cuprates has recently been used to account for the lack of Bi–O electron pockets around $(\pi, 0)$ in those materials [55].

3.2. Electronic dispersion and Fermi surface by ARPES

Figure 8(b) shows ARPES data[5] from a $T_c = 30$ K very overdoped Tl2201 sample (Tl2201-OD30) taken close to the (0,0)-(π,π) direction in momentum space, the so-called 'nodal' direction where the d-wave superconducting gap is zero. Each line in figure 8(b) is an energy distribution curve (EDC) from a given position in momentum space along the line marked as I in the Fermi surface plot of figure 8(a). These EDCs show a strongly dispersing QP peak, related to the $3d_{x^2-y^2}$ CuO band, which emerges from the background at high binding energies and progressively sharpens as it disperses all the way to the Fermi energy E_F. Note that, in the following, the term QP is used in a loose sense to identify a 'reasonably sharp' dispersive peak, without precise reference to specific models accounting for correlation effects in a many-body system (more discussion will be given in subsection 3.4 and section 4). From the results of band structure calculations (figure 7), we expect the bottom of this band to be located at the Γ point, or (0,0), at a binding energy of approximately 1 eV with respect to the chemical potential. Although it is hard to track the band all the way down to high binding energies in the raw data, it is possible to highlight the band dispersion by taking a second derivative of the ARPES intensity with respect to energy. This is plotted in figure 8(d) and indicates a filled bandwidth of only $\sim$250 meV, suggesting a renormalization factor of about four between single particle band structure calculations and measured ARPES spectra. Near $(\pi, 0)$, the so-called 'antinodal'

[5] The ARPES experiments were carried out at the Swiss Light Source (SLS) on the Surface and Interface Spectroscopy Beamline [56]–[58] and at the Stanford Synchrotron Radiation Laboratory (SSRL) on Beamline 5–4, in both cases using a Scienta SES-2002 photoelectron spectrometer. At SLS, all measurements were performed with circularly polarized 59 eV photons, and energy and angular resolutions of 24 meV and 0.2°; the data were acquired on a strongly overdoped sample with $T_c = 30$ K (Tl2201-OD30), and a lightly overdoped sample with $T_c = 63$ K (Tl2201-OD63). The samples were cleaved *in situ* at 6×10^{-11} torr and kept at 10 K throughout the measurements. At SSRL, all data were acquired at 28 eV with linearly polarized light and with energy and angular resolutions of 15 meV and 0.35°. The SSRL data were from lightly overdoped samples with $T_c = 74$ K (Tl2201-OD74), which were cleaved at 3×10^{-11} Torr and temperature cycled between 10 and 85 K. Spectra from different momenta were normalized by the k-independent spectral weight measured between 6 and 11 eV binding energy.

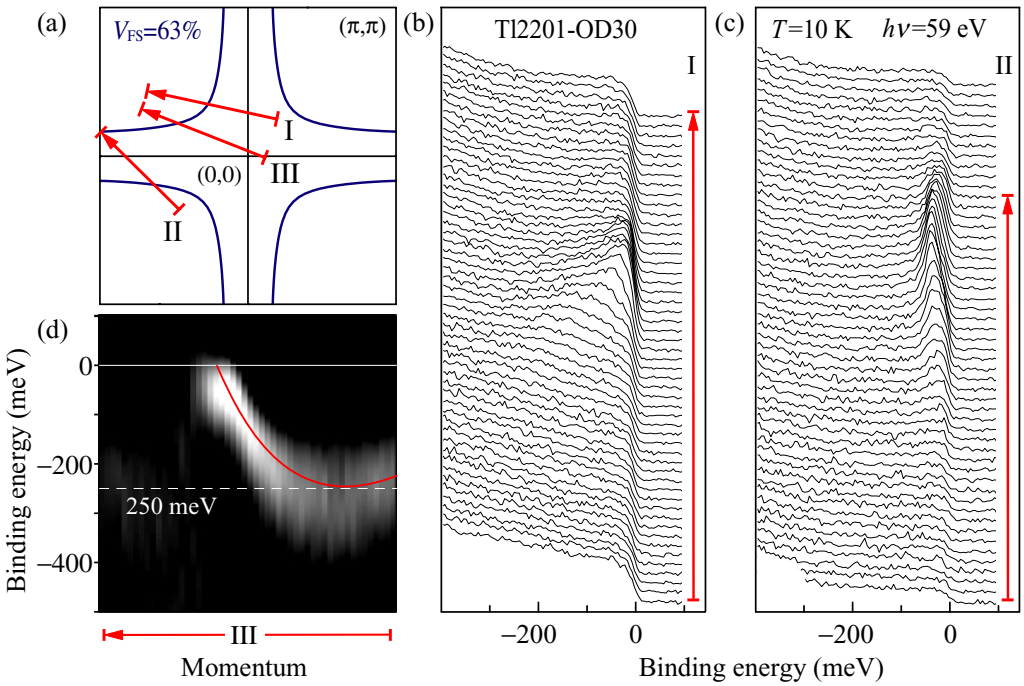

Figure 8. (a) Fermi surface calculated for a 63% Brillouin zone volume, counting holes, as in figure 7(c). (b, c) ARPES spectra taken at $T = 10$ K on Tl2201-OD30 along the directions marked by arrows I and II in (a). (d) Second derivative versus energy of the spectra from along arrow III in (a); the red line is our tight-binding fit (see text for a more detailed description).

direction where the d-wave superconducting gap exhibits its largest value, we also detected well-defined dispersive QP peaks, which define a shallow parabolic band. As mentioned in the discussion of the LDA calculations of figure 7(a), the bottom of this band corresponds to the extended van Hove singularity observed near $(\pi, 0)$ in all HTSC cuprates [3, 4]. At this high doping level, this feature is located approximately 40 meV below the chemical potential, which corresponds to a renormalization factor of about five with respect to the band structure calculations.

The momentum at which a dispersing QP peak is observed to reach E_F and disappear provides ARPES's means of determining a Fermi wavevector k_F. This wavevector identifies one point along the normal state Fermi surface, which is the contour in momentum space that separates filled from empty electronic states and whose existence and details are of fundamental importance for the understanding of the macroscopic physical properties of a material. By integrating the ARPES spectra over a ± 5 meV energy window about E_F for a large number of cuts in momentum space and then plotting the results versus momentum in the 2D projected tetragonal Brillouin zone, one obtains an estimate of the normal-state Fermi surface. This has been done for Tl2201-OD30, and is shown in figure 9(b). The location of the Fermi surface crossings has been determined over more than one quadrant across two different zones, and then downfolded to the first Brillouin zone and four-fold symmetrized to clearly show the detailed shape of the Fermi surface in the reduced zone scheme, with improved signal-to-noise. As expected, there is no indication of a TlO electron pocket around (0,0,0). In principle, given that

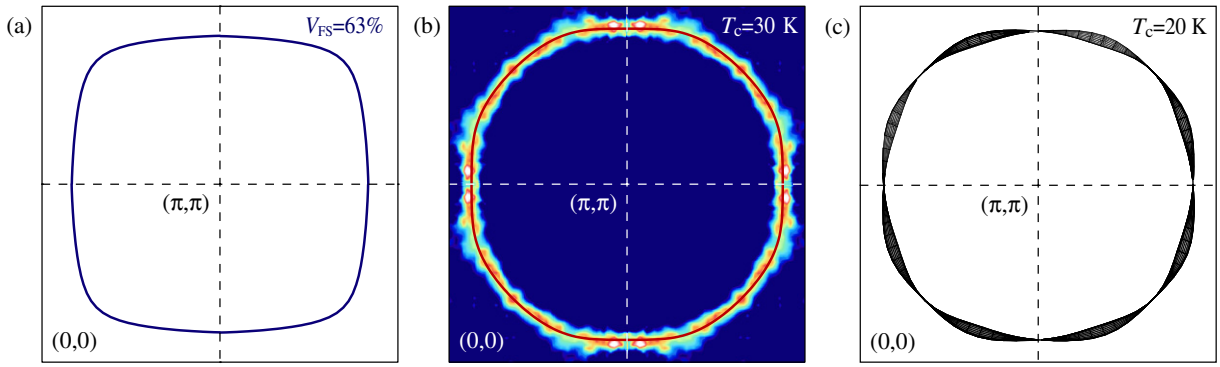

Figure 9. Fermi surfaces, in the projected 2D Brillouin zone, obtained from: (a) band structure calculations (imposing a volume of 63% counting holes, as observed by ARPES on Tl2201-OD30); our (b) ARPES experiments on the $T_c = 30$ K sample (Tl2201-OD30); and (c) the AMRO study on a $T_c = 20$ K Tl2201 crystal by Hussey *et al* [31]. The red line in (b) is the result of our tight-binding fit of ARPES Fermi surface and dispersion; the width of the Fermi surface contour in (c) reflects the magnitude of the c-axis dispersion, here emphasized by a factor of four for clarity [31].

the occupied TlO states should be confined to a small volume around the Γ point, the absence of the TlO pocket in the present ARPES data might simply be the result of having carried out the experiments at k_z values larger than the Fermi wavevector along the c-axis. We checked this possibility by acquiring 2D E_F intensity maps by ARPES as a function of photon energy, which allows one to study the evolution of the Fermi surface upon varying continuously the value of k_z; we have observed, however, no signature of the TlO spheroid over a wide range of photon energies [59]. In conclusion, the Fermi surface determined from this procedure takes the form of a large hole pocket centred at (π,π) with an area that occupies $63 \pm 2\%$ of the Brillouin zone, corresponding to a carrier concentration of 1.26 ± 0.04 hole per Cu atom, or $p = 0.26 \pm 0.04$ greater hole density than the half-filled Mott insulator with 1 hole per Cu atom ($p = 0$ in figure 1). This result is in superb agreement with the recent study of the Fermi surface by angular dependent magnetoresistance oscillation (AMRO) experiments [31], which found a hole-pocket volume of 62% of the Brillouin zone ($p = 0.24$) in a slightly more overdoped $T_c = 20$ K sample (figure 9(a)). The ARPES determination is also in good agreement with the estimates from low temperature measurements of the Hall coefficient, which gave a hole doping of $p = 0.30$ holes/Cu for a $T_c \lesssim 15$ K sample [32].

As a quantitative measure of the shape of the Fermi surface and of the many-body renormalized electronic dispersion, the Tl2201-OD30 ARPES data can be modelled by the tight-binding formula $\epsilon_{\mathbf{k}} = \mu + \frac{t_1}{2}(\cos k_x + \cos k_y) + t_2 \cos k_x \cos k_y + \frac{t_3}{2}(\cos 2k_x + \cos 2k_y) + \frac{t_4}{2}(\cos 2k_x \cos k_y + \cos k_x \cos 2k_y) + t_5 \cos 2k_x \cos 2k_y$ [60], setting $a = 1$ for the lattice constant. With parameters $\mu = 0.2438$, $t_1 = -0.725$, $t_2 = 0.302$, $t_3 = 0.0159$, $t_4 = -0.0805$, $t_5 = 0.0034$, all expressed in eV, this dispersion reproduces both the Fermi surface shape (the solid red line in figure 9(b)), and the QP energy at (0,0) and $(\pi, 0)$ as seen in figures 8(c) and (d). It is worth noting that experimentally the band bottom at $(\pi, 0)$ is extremely flat, a behaviour that could not be reproduced by including only t_1 and t_2 hopping parameters in the model. Alternatively, a simple analytical formula for the 3D electronic dispersion of Tl2201 has recently been derived

within the framework of the linear combination of atomic orbitals (LCAO) approximation [61], and was used to fit both ARPES [33] and AMRO [31] results. A basis set spanning the Cu 4s, Cu $3d_{x^2-y^2}$, O $2p_x$ and O $2p_y$ states was used in order to take into account the effective Cu-Cu hopping amplitude between Cu 4s orbitals in neighbouring CuO_2 layers. This approach emphasizes the significance of the Cu 4s hopping amplitude in obtaining the correct 3D Fermi surface shape, an issue that was originally raised by Andersen *et al* [62]. With regards to the detailed shape of the Fermi surface, LDA band structure calculations predict a more square contour than observed by ARPES and AMRO (figure 9(a)). The inclusion of correlation effects, as well as Cu-Tl substitution or interstitial O-doping beyond a rigid-band picture, might lead to a better agreement; preliminary attempts have not yet led to appreciable improvements [54].

3.3. ARPES study of the superconducting gap

In order for Tl2201 to be a model system to study the overdoped HTSCs by surface and bulk sensitive probes, it is important to show that ARPES measures quantities that are characteristic of the bulk, for both normal and superconducting states. In addition to the quantitative agreement on the normal state Fermi surface, the observation of a superconducting gap in agreement with bulk measurements is also a necessary requirement. In the following, we will discuss three different methods for determining a gap by ARPES. The first two show a gap consistent with a $d_{x^2-y^2}$ form. The third method allows one to follow the temperature dependence of the gap, highlighting the minimal surface degradation that occurs as the temperature is cycled from 10 to 85 K.

The detection of a $d_{x^2-y^2}$ gap using ARPES can be most easily visualized by the comparison of nodal and antinodal symmetrized spectra [63]. The spectra are symmetrized in energy about E_F, by taking $I(\omega) + I(-\omega)$, which minimizes the effects of the Fermi function.[6] While this procedure does not return a quantitative value for the size of the superconducting gap, it provides a qualitative criterion for determining whether or not there is a Fermi crossing, and hence whether or not a superconducting gap has opened along the normal-state Fermi surface. In the symmetrized ARPES data, the presence of a peak in the spectra at E_F indicates a Fermi surface crossing. This procedure has been used extensively for the Bi-based cuprates, both single and bilayer compounds, in detailed investigations of the normal-state Fermi surface, as shown for instance in figures 10(c)–(f) [64], and of the superconducting as well as normal state pseudogap [63, 65]. In the case of our Tl2201-OD30 sample, this crossing is clearly seen in the nodal direction (bold line in figure 10(a)) but not in the antinodal direction (figure 10(b)), which is consistent with a d-wave functional form for the gap.

A more quantitative analysis of the gap can be performed by fitting ARPES spectra along cuts that cross the underlying normal-state Fermi surface, as shown in figure 11. The model used to reproduce the spectra is a Lorentzian peak plus a step-like background. The latter is determined from the ARPES spectra with $k \gg k_F$ and is used to help phenomenologically isolate the coherent part of the spectral function. This lineshape is then multiplied by the Fermi distribution and convolved with the instrumental energy resolution function, to obtain the functional form to be

[6] This procedure assumes that the ARPES spectra are described by $I(\omega) = I_0 f(\omega) A(\mathbf{k}, \omega)$, and that there is particle-hole symmetry for a small range of ω and k about E_F and k_F, such that $A(-\epsilon_{\mathbf{k}}, -\omega) = A(\epsilon_{\mathbf{k}}, \omega)$. With the identity $f(-\omega) = 1 - f(\omega)$, it then follows that $I(\omega) + I(-\omega) = A(\mathbf{k}, \omega)$. It is worth pointing out that this procedure is also valid in the case that energy and momentum resolutions are included in the description of $I(\omega)$, via convolution with the resolution function $R(\Delta k, \Delta\omega)$ [63, 64].

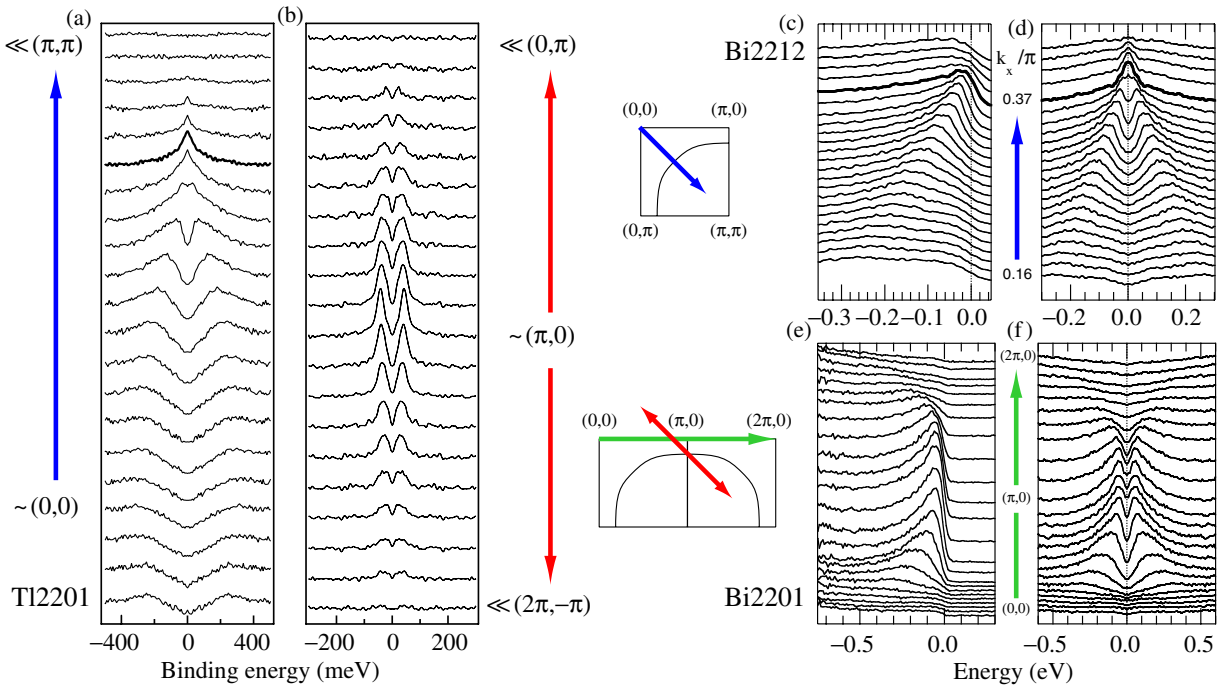

Figure 10. (a, b) Symmetrization of Tl2201-OD30 ARPES spectra from along cuts I and II in figures 8(b) and (c). ARPES spectra and their symmetrization along panels (c) and (d) the nodal direction for overdoped $Bi_2Sr_2CaCu_2O_{8+\delta}$ ($T_c = 88$ K), and (e, f) perpendicular to the antinodal direction for overdoped $Bi_2Sr_2CuO_{6+\delta}$ ($T_c = 23$ K); after [64]. For all samples, the approximate locations of the k-space cuts are indicated in the Brillouin zone sketches. Bold lines in panels (a), (c) and (d) mark the spectra that cross the Fermi energy, identifying a Fermi wavevector k_F; no crossing is observed in panels (b), (e) and (f).

fit to the data [3]. This procedure has been used previously for $Bi_2Sr_2CaCu_2O_{8+\delta}$ [67]. The inset of figure 11(b) shows good agreement between the raw data and the fit. Since heavily overdoped cuprates have weaker, possibly Fermi liquid-like electron correlations, good agreement between the measured QP peak and the Lorentzian is in principle expected.

Figures 11(d) and (e) show the peak positions from the fits compared with our tight-binding description of the normal-state electronic structure near the antinodal region. At higher binding energies, there is good agreement between the fit peak positions and the normal-state dispersion. At lower binding energies, however, the peak does not reach E_F, but instead reaches a minimum at $\Delta_P \simeq 17$ meV and then disperses back to higher binding energy. This behaviour is a hallmark of Bogoliubov QPs in a superconductor, as shown in the sketch of figures 11(f) and (g), for which a beautiful experimental demonstration was recently obtained by ARPES on the trilayer Bi-cuprate $Bi_2Sr_2Ca_2Cu_3O_{10+\delta}$ [66]. Simultaneously, we observe a reduction of spectral weight, by about a factor of 2, when the QP peak has dispersed from the van Hove singularity all the way to k_F. This is consistent with the spectral intensity of Bogoliubov QPs being determined by the coherence factor $v_{\mathbf{k}}^2 = 1 - u_{\mathbf{k}}^2 = \frac{1}{2}(1 - \epsilon_{\mathbf{k}}/E_{\mathbf{k}})$, with $E_{\mathbf{k}} = \sqrt{\epsilon_k^2 + \Delta_{\mathbf{k}}^2}$, which corresponds to 1/2 when $\epsilon_{\mathbf{k}} = \epsilon_{\mathbf{k}_f} = 0$ and 1 for $|\epsilon_{\mathbf{k}}| \gg \Delta_{\mathbf{k}}$. Extending this analysis to other momenta along the Fermi surface, one can study the k-dependence of the gap: at $\sim (\pi/2, \pi/2)$ the peak does

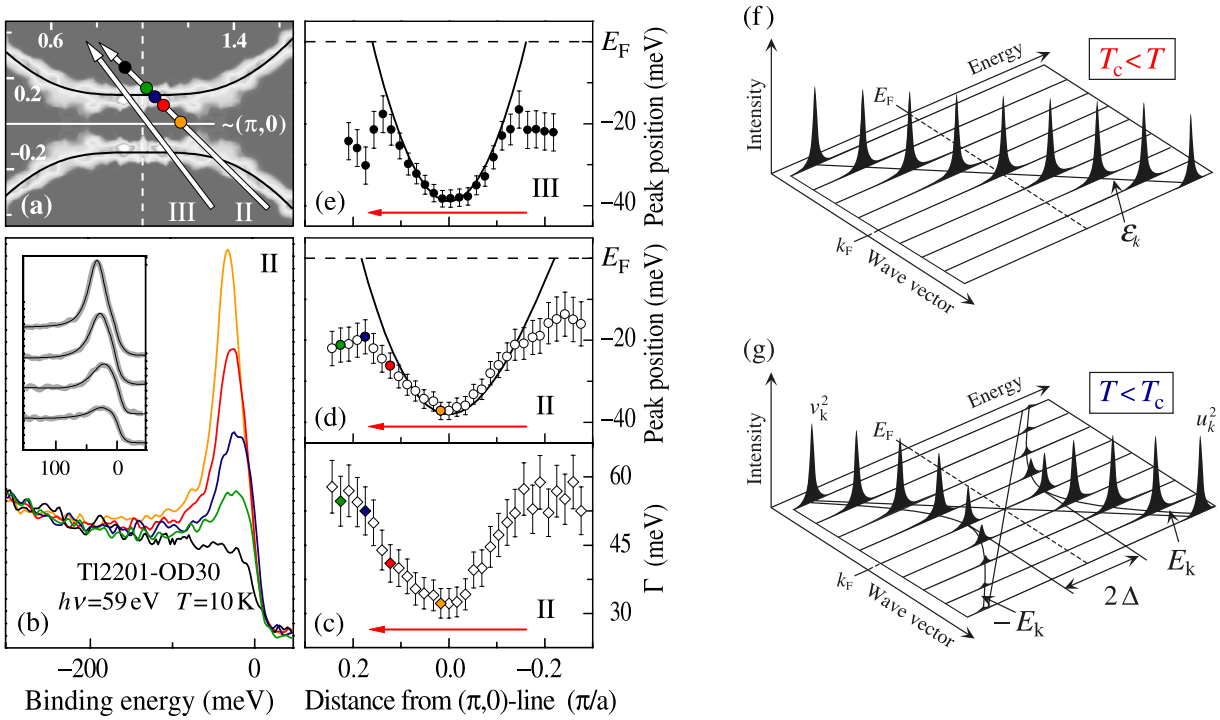

Figure 11. (a) Fermi surface of Tl2201-OD30 near $(\pi, 0)$. (b) Selected spectra from along cut II in (a); their k-space positions are indicated by circles of corresponding colour. (c), (d) QP linewidth Γ and peak position from a Lorentzian fit of the EDCs along cut II in (a). (e) Similarly, QP peak position along cut III in (a). Black lines in (a), (d) and (e) are our tight-binding results. (f) Normal and (g) superconducting state single-particle spectral function, highlighting particle-hole mixing and backward dispersion of Bogoliubov QPs below T_c (after [66]).

cross E_F (not shown), while at intermediate momenta a gap smaller than at $(\pi, 0)$ is observed, as on the right-hand side of figure 11(d), consistent with d-wave symmetry.

The temperature dependence of the gap at the antinode has been measured for Tl2201-OD74. Figures 12(a) and (b) present symmetrized ARPES data along the $(\pi, 0) - (\pi, \pi)$ direction, at temperatures above and below T_c. In exactly the same manner as the k-dependent symmetrized data of figures 10(a) and (b), the temperature-dependent data of figures 12(a) and (b) show a clear gap at $k = k_F$ at 10 K, which is smaller at 85 K (with this type of analysis, the broadness of the QP peak and noise level make it hard to conclude whether the gap has completely closed at 85 K). Figure 12(c) shows EDCs averaged over a narrow k-range around k_F at 10, 45, 85, and again at 10 K. The opening of the superconducting gap is indicated by the shift of the EDC leading-edge midpoint (LEM) to binding energies higher than the chemical potential for $T < T_c$, which defines the so-called LEM gap. The inset of figure 12(c) shows a closer view of these k-integrated EDCs around E_F, together with 10 K polycrystalline Au data and the simulation of an energy-resolution broadened Fermi function at 85 K, which provide a reference for a normal-metal angle-integrated spectrum. It is clear from this figure that, as temperature increases, the size of the gap decreases although it does not seem to completely close at 85 K. This is suggested by comparing the position of the LEM of the 85 K ARPES data with the simulated Fermi function;

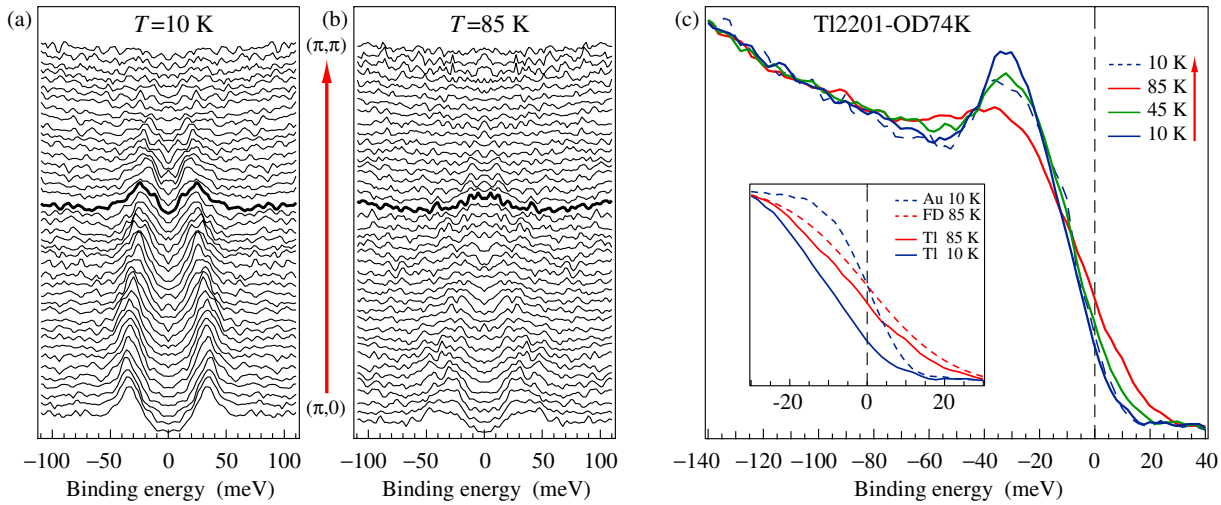

Figure 12. Symmetrized ARPES spectra measured at (a) 10 K and (b) 85 K on Tl2201-OD74 along $(\pi, 0)$–(π, π). Bold lines indicate the EDCs closest to k_F. (c) The k integrated spectral weight at the antinode, for several temperatures; an enlarged view of the leading edge is given in the inset, together with a 10 K Au Fermi edge and an 85 K resolution-broadened Fermi function.

they are close in energy but not quite coincident. It is possible that there is still a pseudogap at temperatures slightly above $T_c = 74$ K at this doping level. It is worth emphasizing that as the temperature is lowered back to 10 K, the gap reopens to approximately the same size. Although a partial degradation of the ARPES features can be seen, the QP peaks and the gap are still clearly observable. This is strong evidence that the surface is stable under these experimental conditions and is thus suitable for detailed surface-sensitive experiments. From these data, a superconducting peak (SCP) position of ∼33 meV and an LEM gap of ∼15 meV can be extracted (for the more overdoped Tl2201-OD30 sample, we obtained ∼17 meV and 8 meV, respectively [33]).

As a direct comparison with other cuprates and different means of determining the gap, figures 13(a) and (b) present a compilation of the doping dependence of the gap magnitude. Figure 13(a) refers only to spectroscopic studies of optimally and overdoped HTSCs, for which the gap is proportional to T_c. Our results from Tl2201-OD74 and Tl2201-OD30 are fully consistent with the behaviour observed on the other cuprates, as far as both SCP and LEM positions are concerned. Even more significant is figure 13(b), which demonstrates that ARPES measures gap values that follow the same trend as those derived from thermal conductivity, a bulk transport property. A more accurate comparison would require an analysis of the ARPES data beyond the mere determination of SCP and LEM positions, for instance on the basis of a model spectral function; this is however complicated by the non-trivial doping dependence of the ARPES data, and in the present case was done for Tl2201-OD30 but not Tl2201-OD74.

3.4. ARPES lineshape analysis

The electrical and thermal transport properties suggest that overdoped Tl2201 may be regarded as a Fermi liquid [27, 31, 32]. Since the ARPES data for both the normal and superconducting states indicate that single-particle surface-sensitive probes do provide information representative

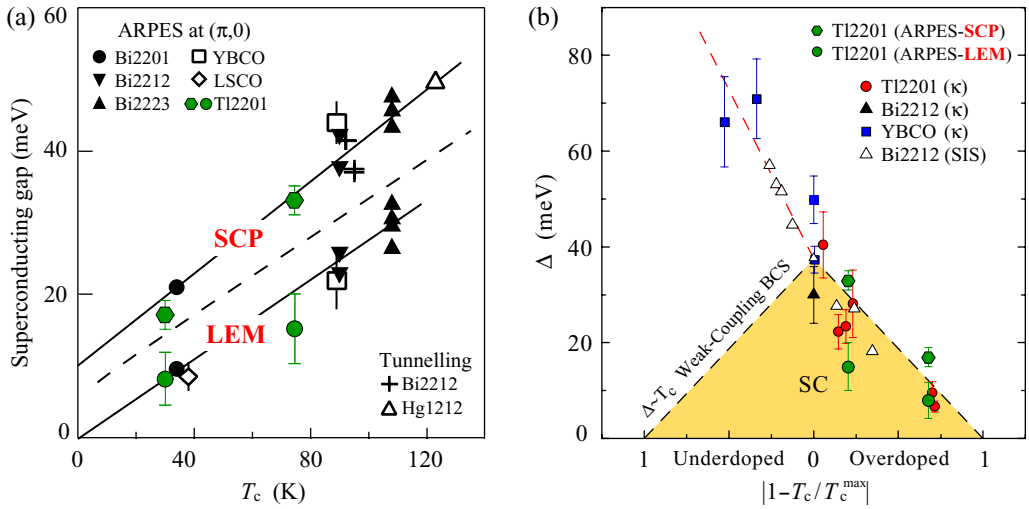

Figure 13. (a) Superconducting gap magnitude estimated by tunnelling and ARPES from the SCP and the LEM shift, plotted versus T_c for various optimally or overdoped cuprates (after [68]). (b) Gap values from thermal conductivity, tunnelling, and ARPES plotted versus $|1 - T_c/T_c^{max}|$ for many HTSCs across the phase diagram (after [51]); dashed lines are guides to the eye. Both plots include our own Tl2201-OD74 and Tl2201-OD30 ARPES results.

of the bulk, overdoped Tl2201 might be an ideal material for a quantitative study of the strength and nature of the many-body effects, which are revealed by the energy and momentum evolution of a QP's intrinsic ARPES lineshape [6]. In general, however, the shape of an ARPES peak does not correspond directly to an excitation's intrinsic lineshape. This is primarily due to an extrinsic contribution from momentum and energy resolution of the analyzer. A recent study on the model 2D Fermi liquid system Sr_2RuO_4 highlights the significant issues involved in removing the effects of the analyzer resolution [69]; in particular, it clearly shows that both the linewidth and the peak position can be affected by resolution effects. There are significant challenges to completely removing the analyser resolution from the data and stringent requirements on the data quality needed to attempt such analysis; therefore, we will analyse the current Tl2201 spectra in a more qualitative and phenomenological manner, concentrating primarily on the momentum dependence of the QP peaks measured in the superconducting state for different doping levels.

Beyond the issue of the experimental resolution, matrix element effects and the handling of the ARPES background are the two main complications in attempting even a qualitative description of the momentum dependence of the QP lineshapes. Experimentally, problems due to matrix element effects may be reduced by appropriate choice of measurement conditions such as geometry, photon energy, and polarization. For the experiments performed at the SLS and the data discussed in the following, circularly polarized 59 eV photons were used. Circular polarization was chosen specifically to minimize matrix element effects which, using symmetry arguments, can be shown to be most extreme for linear polarization [3]. The photon energy was selected based on our experience on other cuprates—specifically $La_{2-x}Sr_xCuO_4$ (LSCO), where similar photon energies were used to reveal structure that had previously been missed in lower-energy ARPES data [24, 70]. Finally, in order to gain more reliable information, the ARPES data were taken over multiple Brillouin zones, making it possible to verify that, for the same point

in the reduced zone scheme, the lineshapes from different zones in the extended zone scheme were qualitatively the same.

The most commonly used method to isolate a QP peak from the experimental background [3, 71], is to subtract a phenomenological ARPES background determined from the data at k-values far removed from those at which the QP-like peaks are detected. In our analysis we will use this approach, taking as background the weakly k-dependent photoemission intensity observed in each momentum space cut for $k \gg k_F$. The fundamental problem with this approach is that if some of the background is related to the incoherent part of the spectral function, as one would expect for correlated electron system, then by subtracting the background we are actually disregarding some of the most crucial information contained in the ARPES spectra. In fact, the k- and ω-dependence of the incoherent part of the spectral function is, in many respects, as important as the behaviour of the QP peak itself; unfortunately we do not yet have the means to reliably extract information from it.

In figure 8(b), similar to what was previously observed in all photoemission studies of the cuprates [3, 4], we see that in the nodal region the width of the QP peaks increases as a function of binding energy, as expected from simple phase-space arguments. This is, however, in sharp contrast to what is observed in the antinodal region, where the sharpest peak is found at the bottom of the band: in figure 11(c), the linewidth Γ of the QP peak is observed to grow from $\sim$30 to $\sim$55 meV as the QP peak disperses from $\sim$39 to $\sim$20 meV binding energy. Possible origins for this anomalous behaviour will be discussed later, but it should be pointed out that an analogous effect was recently reported for very overdoped and nearly non-superconducting $Bi_{1.74}Pb_{0.38}Sr_{1.88}CuO_{6+\delta}$ [72]. Another striking feature of the lineshape evolution is that the QP peaks are much broader in the *nodal* region than in the *antinodal* region, as evidenced by the direct comparison of figures 8(b) and (c). To elaborate on this, in figure 14(a) we present a compilation of spectra from along the Fermi surface contour, with k slightly smaller than k_F and corresponding to a binding energy of $\sim$35 meV. The choice in favour of spectral peaks at a binding energy lower than E_F is dictated by the need to compare spectra not affected by either the opening of the d-wave gap or the anomalous low-binding-energy broadening seen at the antinode. The sharp peak near $(\pi, 0)$ becomes progressively broader as $(\pi/2, \pi/2)$ is approached. In order to determine whether this apparent broadening represents an increase in the QP linewidth Γ, or is merely a loss of spectral weight, the momentum-independent background from $k \gg k_F$ is subtracted from the ARPES spectra as shown in figure 14(b); then the data are integrated over varying energy ranges and plotted in figure 14(c), normalized at the Fermi surface angle $\alpha = 0°$. For narrow integration windows, there is a drop as a function of α: the QPs show a loss of low-energy weight (and possibly coherence) in the nodal region. However, once the integration window is expanded to about 550 meV, the spectral weight of the QP peaks becomes angle-independent (EDCs from different momenta were normalized by the k-independent spectral weight measured between 6 and 11 eV binding energy). This indicates that the k-dependent broadening of the ARPES spectra reflects a loss of coherence of the QP spectrum rather than matrix element effects.

The observed QP anisotropy of Tl2201-OD30, with peaks much broader in the nodal than the antinodal region, is in sharp contrast to the behaviour observed in underdoped cuprates, where the QP peaks are sharp near $(\pi/2, \pi/2)$ and very broad around $(\pi, 0)$, as summarized in figure 17. As doping is increased, the antinodal QP peaks sharpen but remain significantly broader than the nodal QPs up to optimal doping, at least in the normal state. Even in the superconducting state, where antinodal QPs sharpen considerably, the ARPES lineshapes for underdoped and

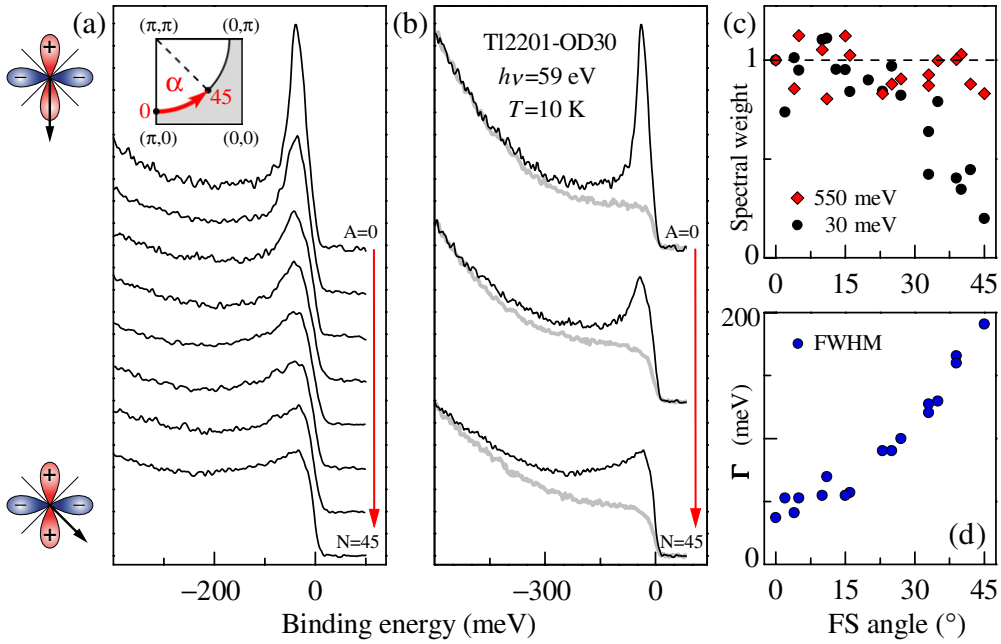

Figure 14. (a) Tl2201-OD30 ARPES spectra at k slightly smaller than k_F along the Fermi surface contour (corresponding to a QP binding energy of ∼35 meV). (b) Selected spectra from (a) along with their corresponding $k \gg k_F$ background. (c) Spectral weight of the background subtracted spectra, integrated over different energy ranges and normalized with respect to the $\alpha = 0$ antinodal value, plotted versus the Fermi-surface angle α. (d) QP linewidth Γ plotted versus the Fermi-surface angle α. Nodal and antinodal momenta are here indicated, as in figure 17, by the red-blue 'butterfly' of the $d_{x^2-y^2}$ order parameter; note, however, that while ARPES can measure the k-dependence of the superconducting gap magnitude, it does not provide any information on the phase, whose determination requires phase sensitive experiments [11].

optimally-doped materials are still highly anisotropic, with a minimum in linewidth at $(\pi/2, \pi/2)$ [3, 4]. Overall this behaviour leads to the expectation that increasing doping beyond the optimal value will simply render the QP linewidths progressively more isotropic. Indeed, isotropic lineshapes were observed on early data from very overdoped, non-superconducting $Bi_{1.80}Pb_{0.38}Sr_{2.01}CuO_{6-\delta}$ [73], although more recent work on the same material [72] exhibits a behaviour more consistent with what is reported here for Tl2201. Going back to the QP anisotropy reversal observed for Tl2201-OD30 in figure 14, and presented again in figure 15(b) for nodal and antinodal points only, it must be emphasized that the same, albeit less pronounced, effect was observed in our Tl2201-OD63 sample, as shown in figure 15(a). For comparison, in the inset of figure 15(a) we have plotted ARPES data from overdoped ($x = p = 0.22$) $La_{2-x}Sr_xCuO_4$ [74]. This sample has $T_c \simeq \frac{2}{3}T_c^{max}$, comparable to the degree of overdoping of our sample Tl2201-OD63, which also has $T_c \simeq \frac{2}{3}T_c^{max}$ for the much larger $T_c^{max} = 93$ K of the Tl2201 family. The data from LSCO exhibit a QP anisotropy similar to that in Tl2201-OD63, suggesting that the observed QP anisotropy reversal might indeed be generic to the overdoped cuprates.

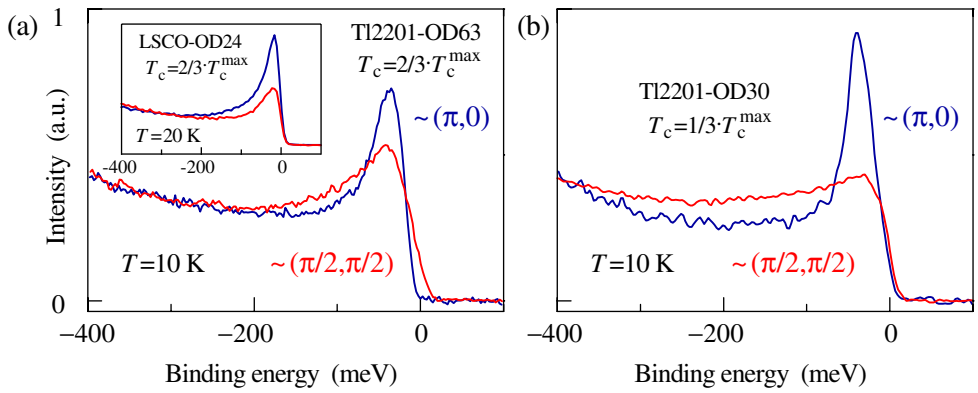

Figure 15. Nodal and antinodal spectra at $k \lesssim k_F$ from (a) Tl2201-OD63, (b) Tl2201-OD30 and (inset) overdoped LSCO-OD24 ($p = 0.22$, from [74]). For both samples in (a), $T_c \simeq \frac{2}{3}T_c^{max}$ with respect to T_c^{max} of each family [25].

Before proceeding to the discussion of the broader significance of these findings, we comment here on two extrinsic effects that could potentially contribute to an anomalous k-dependent broadening of the QP lineshapes: residual k_z electronic dispersion and resolution broadening effects. Firstly, the dispersion of the electronic structure along the c-axis may indeed give rise to $k_{||}$-dependent broadening of the ARPES features [75, 76] (where $k_{||}$ is the ab-plane momentum). This effect could be doping-dependent because there is a 0.4% c-axis lattice constant reduction as doping is increased [47]. However, the k_z-dispersion vanishes in Tl2201 along the $(0, 0)$–(π, π) and $(\pi, 0)$–(π, π) directions, and thus at all nodal and antinodal points. This is a direct consequence of the symmetry of the body-centred tetragonal unit cell, and holds also for LSCO. Figures 16(a) and (b) illustrate this point by showing ARPES data for both materials together with band structure calculations for LSCO [75], and AMRO data for Tl2201 [31]. Along these high-symmetry directions, no k_z-dispersion is present either in the LSCO calculations or the Tl2201 AMRO data (in both cases the k_z-dispersion is proportional to the width of the 2D projected contours). This is consistent with the ARPES maps for the two systems, although the broader E_F intensity patches for LSCO indicate that the 3D character is stronger in LSCO than in Tl2201. A residual k_z dispersion might contribute to the overall width of the ARPES features [75, 76], but it cannot be responsible for the reversal of the anisotropy observed on overdoped cuprates, which has a monotonic $k_{||}$-dependence between $(\pi/2, \pi/2)$ and $\sim (\pi, 0)$.

The second extrinsic effect that influences the width in energy of an ARPES spectrum, or EDC, is instrumental resolution. In a 2D system, the width in energy is determined by the intrinsic inverse lifetime of the QP excitation and by the experimental resolution broadening, which reflects both the energy ($\Delta\omega$) and angular (Δk) resolution of the apparatus [6]. For a dispersionless feature, the instrumental contribution to the total EDC width is determined solely by the energy resolution $\Delta\omega$. However, for a dispersive feature, the angular resolution Δk contributes to the energy broadening in a manner directly proportional to the band velocity ($v_F \neq 0$ in figure 16(c)). Since the Fermi velocity around the Fermi surface of the cuprates is highly anisotropic, varying from approximately 0.5–1.8 eV Å in going from antinodal to nodal region, this should give rise to a momentum-dependent resolution broadening of the EDCs. This broadening would be more severe at the nodes, where v_F is at its largest, which raises the concern

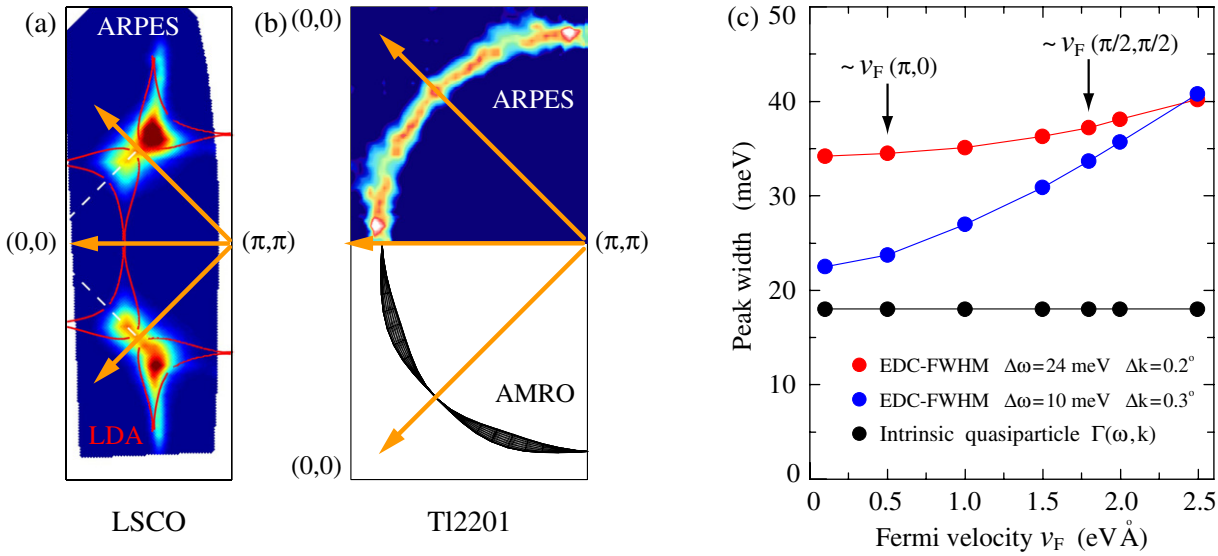

Figure 16. (a) ARPES intensity map for emission from E_F for overdoped LSCO-OD24 ($p = 0.22$). Red lines are the calculated 3D Fermi surface for $k_z = 0$ and π/c; the enclosed area is the projection of the Fermi surface onto the 2D k_x-k_y plane, and denotes the region allowed for emission [75]. (b) ARPES and AMRO [31] data from Tl2201 (for $p = 0.26$ and 0.24, respectively). In (a) and (b) the yellow arrows identify directions characterized by zero k_z dispersion as indicated by the LDA calculations and consistent with AMRO experiments, which also suggest much weaker residual 3D effects in Tl2201 than in LSCO. (c) Resolution contributions to the width of an ARPES EDC calculated, as a function of Fermi velocity v_F, from the 2D convolution of a Lorentzian QP peak (binding energy $\omega = 30$ meV and intrinsic width $\Gamma = 18$ meV) with Gaussian energy and momentum resolution functions (results corresponding to our experimental parameters are in red).

that the larger nodal widths shown in figures 14 and 15 might be an artefact of the instrumental resolution. We have carefully evaluated the contribution of resolution broadening effects for our experimental conditions with a variety of different procedures and the results are summarized in figure 16(c). For our experimental parameters (red data, $\Delta\omega = 24$ meV and $\Delta k = 0.3°$) the k-dependent resolution broadening is of the order of few meV, nowhere near the factor of four observed in figure 14(d).

4. Discussion and conclusions

Using a self-flux method and partial encapsulation, we have grown single crystals of the single-layer overdoped cuprate superconductor Tl2201. The crystals were annealed under controlled oxygen partial pressures to set a homogeneous doping level whilst preventing decomposition, and typically exhibited sub-Kelvin superconducting transition widths as measured in a SQUID magnetometer. Their high quality and homogeneity were evidenced not only by these narrow

transition widths but also by their extremely narrow rocking curve widths, comparable to $YBa_2Cu_3O_{7-\delta}$ grown in YSZ crucibles [48]. An EPMA study found the crystals to have the composition $Tl_{1.884(6)}Ba_2Cu_{1.11(1)}O_{6+\delta}$, which was homogeneous and was not observed to vary between crystals. This level of cation substitution is similar to that reported earlier for single crystals of Tl2201. For higher dopings (i.e. lower T_cs), the crystals were found to be orthorhombic, a slight deviation from a square-planar lattice that is often associated with the unsubstituted phase which has only been prepared in ceramics. The orthorhombic distortion appears to be suppressed by cation disorder, but stabilized by the oxygen interstitials that increase the doping.

While these crystals constitute a significant step forward, much optimization of the growth technique remains, and there is still the challenge of growing single crystals without the cation disorder in the Tl layer. Still, the high quality Tl2201 single crystals grown as part of this effort have enabled the first successful ARPES experiments for this compound [33]. The results on the Fermi surface of Tl2201 mark an important new starting point for understanding the cuprates, namely that there is a material where both a surface-sensitive single-particle spectroscopic technique (ARPES) and comparable bulk transport measurements (AMRO) have arrived at quantitative agreement on a major feature of the normal state [31, 33]. This is a first for the copper-oxide HTSCs and, within the more general class of 3d and 4d transition metal oxides, it is second only to the case of Sr_2RuO_4 for which a similar quantitative agreement was reached between de Haas–van Alphen [77, 78] and ARPES [69], [79]–[82]. The detailed agreement on the Fermi surface (figure 9), together with the good quantitative agreement achieved for the superconducting gap by thermal conductivity and ARPES (figure 13), establishes Tl2201 as an ideal system to study the overdoped regime of the cuprate phase diagram with a wide spectrum of techniques. Next it will be important to study the single-particle excitation spectrum with both ARPES and STS in enough detail to compare to other normal state properties, thus critically testing whether or not a conventional Fermi-liquid description of the electronic properties captures the physics of the normal metal in the heavily overdoped regime. In this regard, it is important to elaborate on the most surprising result that emerged from this study of overdoped Tl2201 by ARPES, one which is counterintuitive within the realm of Fermi liquid theory: the QP anisotropy reversal observed across optimal doping (figures 14 and 15).

A summary of the momentum anisotropy as seen by ARPES in under and overdoped cuprates is given in figure 17, where data from $Ca_{2-x}Na_xCuO_2Cl_2$ [8], for several doping levels, and Tl2201 are directly compared. Early magnetotransport experiments on very overdoped Tl2201, for which a small magnetoresistance and a weak T-dependence of the resistivity and cotangent of the Hall angle have been observed, do not support the presence of strongly k-dependent low-temperature scattering rates in the normal state [32]. More recently, a temperature, doping, and magnetic field dependent AMRO study of Tl2201 suggested a two-component scattering rate consisting of an isotropic T^2 term as well as an anisotropic T-linear term [83], which vanishes at the nodes and has a maximum near the antinodes. The anisotropic term becomes weaker upon overdoping the material, which is consistent with the view that as hole doping increases, the antinodal QPs should gain coherence faster than the nodal ones, eventually leading to a relatively small and fully isotropic scattering rate. Therefore, what is at variance between the ARPES and AMRO results from Tl2201 is not the behaviour of the antinodal QPs, which in both cases are indeed gaining coherence upon overdoping, but rather that the nodal QPs seen in ARPES become progressively less coherent. In addition, on a more quantitative level, one should realize that the overall magnitude of the scattering rate seen by ARPES is approximately a factor of 10 larger than estimated by AMRO.

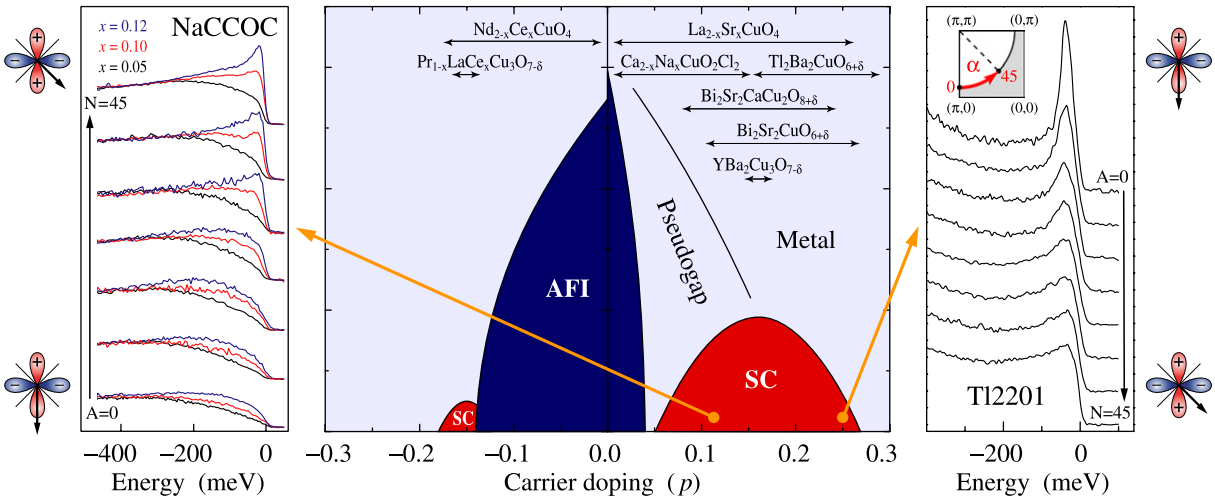

Figure 17. Nodal-antinodal QP anisotropy reversal observed in the cuprates across optimal doping. In underdoped cuprates (e.g. data from $Ca_{2-x}Na_xCuO_2Cl_2$, after [8]) sharp QPs are observed at the nodes (N) and ill-defined QPs at the antinodes (A). In overdoped Tl2201, this behaviour is reversed.

What could be the origin for this discrepancy between ARPES and AMRO determined scattering rates? In this regard, it is worth emphasizing that while AMRO experiments are possible on Tl2201 but not on LSCO due to the higher impurity content of the latter, the ARPES features from the two compounds in the overdoped regime are actually quite comparable (figure 15). This seems to point at the fundamental differences between what the two techniques actually probe. One has also to note that while our ARPES experiments were performed in the superconducting state, the AMRO measurements were carried out in the normal state; and the latter is achieved by the application of external magnetic fields as high as 45 T, which might potentially affect the low-energy QP dynamics. As for the reliability of the ARPES data on the specific point of the loss of coherence of nodal QPs at large dopings, it is important to mention that these findings are also supported by a preliminary study of overdoped $Bi_2Sr_2CaCu_2O_{8+\delta}$ by STM and STS [84]. From the Fourier analysis of the energy-dependent spatial modulations observed in the tunnelling conductance [85], it was concluded that for strongly overdoped samples, the nodal (i.e. low energy) QP interference signal is no longer visible, consistent with a decoherence of the nodal states [84]. Interestingly, although a precise connection is not yet established, recent terahertz [86] and optical [87, 88] spectroscopy results also suggest an abrupt transition in the low-energy QP dynamics across optimal doping, as evidenced by: (i) the decay time of the transient reflectivity in pump–probe experiments on Bi-cuprates [86]; (ii) the doping dependence of the low-frequency optical spectral-weight redistribution across T_c in Bi-cuprates [87]; (iii) the decrease of the optical scattering rate upon overdoping in Tl2201 [88].

A reconciliation of the results might require consideration of the specific sensitivity of transport probes and single-particle spectroscopies to electronic scattering phenomena. In particular, photoemission and scanning tunnelling are very sensitive to electronic scattering involving small momentum transfer, while transport is rather insensitive to it. A possible source of such scattering could be extended impurities far from the CuO_2 planes [89], such as cation substitution or interstitial oxygen which increase with doping in most cuprates. Recent

calculations show that the inclusion of elastic forward scattering in a d-wave superconductor can lead to an overall increase of the scattering rate in the normal state, but also to a strong enhancement of antinodal QP coherence in the superconducting state [90]. A very different model, based on the description of unitary-limit scattering beyond the Born approximation so as to account for multiple scattering from a single point-like impurity, would also lead to loss of nodal coherence and enhancement of antinodal coherence below T_c [91]. However, both models predict an approximately isotropic QP scattering above T_c, as well as temperature dependent effects limited to the energy scale of the gap itself. To test the applicability of these scenarios to the present case, a thorough temperature dependent study is required. Finally, it should also be pointed out that sources of scattering relevant to this discussion are not just limited to impurities; inelastic (i.e. electronic) scattering involving small momentum transfer might also result in anomalous decoherence of the nodal QPs. For instance, low-energy (i.e. small q) quantum-critical fluctuations associated with proximity to a competing superconducting $d_{x^2-y^2} + id_{xy}$ phase [92], or a ferromagnetic phase, could also lead to a similar QP anisotropy reversal [93].

Acknowledgments

We gratefully acknowledge D G Hawthorn, K M Shen, N E Hussey, A P Mackenzie, J C Davis, D J Scalapino, and G A Sawatzky for discussions and M Platé, N P Armitage, A B Kuzmenko, S Chiuzbaian, M Shi, M Falub and L Patthey for assistance during the ARPES experiments. We are also grateful to machine and beamline groups at the Swiss Light Source and Stanford Synchrotron Radiation Laboratory, whose outstanding efforts made the experiments possible. This study was supported by the Natural Sciences and Engineering Research Council of Canada (NSERC), Canada Foundation for Innovation (CFI), Canadian Institute for Advanced Research (CIAR) Quantum Materials Program, British Columbia Synchrotron Institute (BCSI) and Canada Research Chairs Program (AD).

References

[1] Orenstein J and Millis A J 2000 Advances in the physics of high-temperature superconductivity *Science* **288** 468–74

[2] March 2006 Special issue on high-temperature superconductors *Nat. Phys.* **2** 133–210

[3] Damascelli A, Hussain Z and Shen Z-X 2003 Angle-resolved photoemission studies of the cuprate superconductors *Rev. Mod. Phys.* **75** 473–541

[4] Campuzano J C, Norman M R and Randeria M 2004 *Photoemission in the High T_c Superconductors* vol II, pp 167–265 (Berlin: Springer)

[5] Fischer Ø, Kugler M, Maggio-Aprile I, Berthod C and Renner C 2006 *Rev. Mod. Phys.* at press (*Preprint* cond-mat/0610672)

[6] Damascelli A 2004 Probing the electronic structure of complex systems by ARPES *Phys. Scr.* T **109** 61–74

[7] Hanaguri T, Lupien C, Kohsaka Y, Lee D H, Asuma M, Takano M, Takagi H and Shen Z-X 2004 A 'checkerboard' electronic crystal state in lightly hole-doped $Ca_{2-x}Na_xCuO_2Cl_2$ *Nature* **430** 1001–1005

[8] Shen K M *et al* 2005 Nodal quasiparticles and antinodal charge ordering in $Ca_{2-x}Na_xCuO_2Cl_2$ *Science* **307** 901–904

[9] Smadici S, Abbamonte P, Taguchi M, Kohsaka Y, Sasagawa T, Azuma M, Takano M and Takagi H 2006 Absence of long-ranged charge order in $Na_xCa_{2-x}CuO_2Cl_2$ at $x = 0.08$ *Preprint* cond-mat/0603671

[10] Hardy W N, Bonn D A, Morgan D C, Liang R and Zhang K 1993 Precision measurements of the temperature dependence of λ in $YBa_2Cu_3O_{6.95}$: strong evidence for nodes in the gap function *Phys. Rev. Lett.* **70** 3999–4002

[11] Tsuei C C and Kirtley J R 2000 Pairing symmetry in cuprate superconductors *Rev. Mod. Phys.* **72** 969–1016

[12] Kirtley J R, Tsuei C C, Ariando A, Verwijs C J M, Harkema S and Hilgenkamp H 2006 Angle-resolved phase-sensitive determination of the in-plane gap symmetry in $YBa_2Cu_3O_{7-\delta}$ *Nat. Phys.* **2** 190–4

[13] Bonn D A and Hardy W N 1996 *Physical Properties of High Temperature Superconductors* ed Ginsberg D M (Singapore: World Scientific) chapter 2 p 7

[14] Hill R W *et al* 2004 Transport in ultraclean $YBa_2Cu_3O_7$: neither unitary nor Born impurity scattering *Phys. Rev. Lett.* **92** 027001

[15] Basov D N and Timusk T 2005 Electrodynamics of high-T_c superconductors *Rev. Mod. Phys.* **77** 721–79

[16] Devereaux T P and Hackl R 2006 Inelastic light scattering from correlated electrons *Rev. Mod. Phys.* at press (*Preprint* cond-mat/0607554)

[17] Eschrig M 2006 The effect of collective spin-1 excitations on electronic spectra in high-T_c superconductors *Adv. Phys.* **55** 47–183

[18] Tranquada J M 2007 Neutron scattering studies of antiferromagnetic correlations in cuprates *Handbook of High Temperature Superconductivity: Theory and Experiment* ed J R Schrieffer (Berlin: Springer) at press (*Preprint* cond-mat/0512115)

[19] Derro D J, Hudson E W, Lang K M, Pan S H, Davis J C, Markert J T and de Lozanne A L 2002 Nanoscale one-dimensional scattering resonances in the CuO chains of $YBa_2Cu_3O_{6+x}$ *Phys. Rev. Lett.* **88** 097002

[20] Schabel M C, Park C-H, Matsuura H, Shen Z-X, Bonn D A, Liang R and Hardy W N 1998 Angle-resolved photoemission on untwinned $YBa_2Cu_3O_{6.95}$. I. Electronic structure and dispersion relations of surface and bulk bands *Phys. Rev.* B **57** 6090

[21] Lu D H *et al* 2001 Superconducting gap and strong in-plane anisotropy in untwinned $YBa_2Cu_3O_{7-\delta}$ *Phys. Rev. Lett.* **86** 4370–3

[22] Borisenko S V *et al* 2006 Kinks, nodal bilayer splitting, and interband scattering in $YBa_2Cu_3O_{6+x}$ *Phys. Rev. Lett.* **96** 117004

[23] Maggio-Aprile I, Renner Ch, Erb A, Walker E and Fischer Ø 1995 Direct vortex lattice imaging and tunneling spectroscopy of flux lines on $YBa_2Cu_3O_{7-\delta}$ *Phys. Rev. Lett.* **75** 2754–7

[24] Zhou X J, Cuk T, Devereaux T, Nagaosa N and Shen Z-X 2007 Angle-resolved photoemission spectroscopy on electronic structure and electron-phonon coupling in cuprate superconductors *Handbook of High Temperature Superconductivity: Theory and Experiment* ed J R Schrieffer (Berlin: Springer) at press (*Preprint* cond-mat/0604284)

[25] Eisaki H, Kaneko N, Feng D L, Damascelli A, Mang P K, Shen K M, Shen Z-X and Geven M 2004 Effect of chemical inhomogeneity in bismuth-based copper oxide superconductors *Phys. Rev.* B **69** 064512

[26] Chaio M, Hill R W, Lupien C, Taillefer L, Lambert P, Gagnon R and Fournier P 2000 Low-energy quasiparticles in cuprate superconductors: a quantitative analysis *Phys. Rev.* B **62** 3554–8

[27] Proust C, Boaknin E, Hill R W, Taillefer L and Mackenzie A P 2002 Heat transport in a strongly overdoped cuprate: fermi liquid and a pure *d*-wave BCS superconductor *Phys. Rev. Lett.* **89** 147003

[28] Wagner J L, Chmaissem O, Jorgensen J D, Hinks D G, Radaelli P G, Hunter B A and Jensen W R 1997 Multiple defects in overdoped $Tl_2Ba_2CuO_{6+\delta}$: effects on structure and superconductivity *Physica* C **277** 170–82

[29] Tsuei C C, Kirtley J R, Ren Z F, Wang J H, Raffy H and Li Z Z 1997 Pure $d_{x^2-y^2}$ order-parameter symmetry in the tetragonal superconductor $Tl_2Ba_2CuO_{6+\delta}$ *Nature* **387** 481–3

[30] He H, Bourges P, Sidis Y, Ulrich C, Regnault L P, Pailhes S, Berzigiarova N S, Kolesnikov N N and Keimer B 2002 Magnetic resonant mode in the single-layer high-temperature superconductor $Tl_2Ba_2CuO_{6+\delta}$ *Science* **295** 1045–7

[31] Hussey N E, Abdel-Jawad M, Carrington A, Mackenzie A P and Ballcas L 2003 A coherent three-dimensional Mermi surface in a high-transition-temperature superconductor *Nature* **425** 814–17

[32] Mackenzie A P, Julian S R, Sinclair D C and Lin C T 1996 Normal-state magnetotransport in superconducting $Tl_2Ba_2CuO_{6+\delta}$ to millikelvin temperatures *Phys. Rev.* B **53** 5848–55

[33] Platé M *et al* 2005 Fermi surface and quasiparticle excitations of overdoped Tl2201 by ARPES *Phys. Rev. Lett.* **95** 077001

[34] Siegal M P, Venturini E L, Morosin B and Aselage T L 1997 Synthesis and properties of Tl–Ba–Ca–Cu–O superconductors *J. Mater. Res.* **12** 2825–54

[35] Jondo T K, Abraham R, Cohen-Adad M T and Jorda J L 1992 The BaO–$TlO_{1.5}$ system *J. Alloys Compounds* **186** 347–59

[36] Hasegawa M, Takei H, Izawa K and Matsuda Y 2001 Crystal growth techniques for Tl-based cuprate superconductors *J. Cryst. Growth* **229** 401–4

[37] Tyler A 1998 An Investigation into the Magnetotransport Properties of Layered superconducting perovskites *PhD thesis* University of Cambridge

[38] Liu R S, Hughes S D, Angel R J, Hackwell T P, Mackenzie A P and Edwards P P 1992 Crystal structure and cation stoichiometry of superconducting $Tl_2Ba_2CuO_{6+\delta}$ single crystals *Physica* C **198** 203–8

[39] Hasegawa M, Matsushita Y, Iye Y and Takei H 1994 Growth and anisotropic superconducting properties of $Tl_2Ba_2CuO_6$ and $Tl_2Ba_2CaCu_2O_8$ single crystals *Physica* C **231** 161–6

[40] Kolesnikov N N, Kulakov M P, Molchanov V N, Schegolev I F, Shibaeva R P, Simonov V I, Tamazyan R A and Vyasilev O M 1992 Comparative study of Tl-2201 single crystals with $T_c = 30$ and 110 K by means of x-ray structural analysis and NMR *Physica* C **242** 385–92

[41] Vyasilev O M, Kolesnikov N N, Kulakov M P and Schegolev I F 1992 Tl NMR study of $Tl_2Ba_2CuO_x$ single crystals with various T_c *Physica* C **199** 50–8

[42] Kolesnikov N N, Korotkov V E, Kulakov M P, Molchanov V N, Tamazyan R A and Simonov V I 1992 Structure of superconducting single crystals of 2201 thallium cuprate $(Tl_{1.85}Cu_{0.15})Ba_2CuO_6$, $T_c = 110$ K *Physica* C **195** 219–24

[43] Opagiste C, Triscone G, Couach M, Jondo T K, Jorda J-L, Junod A, Khoder A F and Muller J 1993 Phase diagram of the $Tl_2Ba_2CuO_6$ compounds in the T, p (O_2) plane *Physica* C **213** 17–25

[44] Raveau B, Michel C, Mercey B, Hamet J F and Hervieu M 1995 Crystal chemistry of superconducting copper oxycarbonates *J. Alloys Compounds* **229** 134

[45] Jorda J L, Jondo T K, Abraham R, Cohen-Adad M T, Opagiste C, Couach M, Khoder A and Sibieude F 1993 Preparation of pure $Tl_2Ba_2CuO_{6\pm x}$: the contribution of phase equilibrium studies *Physica* C **205** 177–85

[46] Pouchou J L and Pichoir F 1985 *PAP $\varphi(\rho Z)$ Procedure for Improved Quantitative Microanalysis*, pp 104–6 (San Francisco: San Francisco Press)

[47] Shimakawa Y, Kubo Y, Manako T and Igarashi H 1990 Neutron-diffraction study of $Tl_2Ba_2CuO_{6+\delta}$ with various T_c's from 0 to 73 K *Phys. Rev.* B **42** 10165–71

[48] Liang R, Bonn D A and Hardy W N 1993 Growth of high-quality YBCO single crystals using $BaZrO_3$ crucibles *Physica* C **304** 105–111

[49] Shimakawa Y 1993 Chemical and structural study of tetragonal and orthorhombic $Tl_2Ba_2CuO_6$ *Physica* C **204** 247–61

[50] Parise J B, Torardi C C, Subramanian M A, Gopalakrishnan J and Sleight A W 1989 Superconducting $Tl_{2.0}Ba_{2.0}CuO_{6+\delta}$: a high resolution neutron powder and single crystal x-ray diffraction investigation *Physica* C **159** 239–44

[51] Hawthorn D G *et al* 2006 The quasiparticle gap in $Tl_2Ba_2CuO_{6+\delta}$ from low-temperature thermal conductivity *Preprint* cond-mat/0502273

[52] Andersen O K 1975 Linear methods in band theory *Phys. Rev.* B **12** 3060

[53] Singh D J and Pickett W E 1992 Electronic characteristics of $Tl_2Ba_2CuO_6$ Fermi surface, positron wavefunction, electric field gradients, and transport parameters *Physica* C **203** 193–202

[54] Sahrakorpi S, Lin H, Markiewicz R S and Bansil A 2006 Effect of hole doping on the electronic structure of Tl2201 *Preprint* cond-mat/0607132

[55] Lin H, Sahrakorpi S, Markiewicz R S and Bansil A 2006 Raising Bi-O bands above the Fermi energy level of hole-doped $Bi_2Sr_2CaCu_2O_{8+\delta}$ and other cuprate superconductors *Phys. Rev. Lett.* **96** 097001

[56] Schmidt T, Ingold G, Imhof A, Patterson B D, Patthey L, Quitmann C, Schultze-Breise C and Abela R 2001 Insertion devices at the Swiss Light Source (phase I) *Nucl. Instrum. Methods Phys. Res.* A **467-468** 126–9

[57] Fleshig U, Patthey L and Quitmann C 2001 Extended SX-700 type monochromator combining normal and grazing incidence optics for a new undulator beamline at SLS *Nucl. Instrum. Methods Phys. Res.* A **467-468** 479–81

[58] See also http://sls.web.psi.ch/view.php/beamlines/sis/

[59] Mottershead J D F and Damascelli A 2006 in preparation

[60] Norman M R 2001 Magnetic collective mode dispersion in high-temperature superconductors *Phys. Rev.* B **63** 092509

[61] Mishonov T, Savona S and Stoev M 2005 LCAO model for 3D Fermi surface of high-T_c cuprate $Tl_2Ba_2CuO_{6+\delta}$ *Preprint* cond-mat/0504290

[62] Andersen O K, Liechtenstein A I, Jepsen O and Paulsen F 1995 LDA energy bands, low-energy hamiltonians, t', t'', $t_\perp(k)$, and $J_\perp$ *J. Phys. Chem. Solids* **56** 1573–91

[63] Norman M R *et al* 1998 Destruction of the Fermi surface in underdoped high-T_c superconductors *Nature* **392** 157–60

[64] Mesot J *et al* 2001 Determination of the Fermi surface in high T_c superconductors by angle-resolved photoemission spectroscopy *Phys. Rev.* B **63** 224516

[65] Kanigel A *et al* 2006 Evolution of the pseudogap from Fermi arcs to the nodal liquid *Nat. Phys.* **2** 447–51

[66] Matsui H, Sato T, Wang S-C, Yang H-B, Ding H, Fujii T, Watanabe T and Matsuda A 2003 BCS-like Bogoliubov quasiparticles in high-T_c superconductors observed by angle-resolved photoemission spectroscopy *Phys. Rev. Lett.* **90** 217002

[67] Ding H, Norman M R, Campuzano J C, Randeria M, Bellman A F, Yokoya T, Takahashi T, Mochiku T and Kadowaki K 1996 Angle-resolved photoemission spectroscopy study of the superconducting gap anisotropy in $Bi_2Sr_2CaCu_2O_{8+x}$ *Phys. Rev.* B **54** R9678–R9681

[68] Feng D L *et al* 2002 Electronic structure of the trilayer cuprate superconductor $Bi_2Sr_2Ca_2Cu_3O_{10+\delta}$ *Phys. Rev. Lett.* **88** 107001

[69] Ingle N J C *et al* 2005 Quantitative analysis of Sr_2RuO_4 angle-resolved photoemission spectra: many-body interactions in a model Fermi liquid *Phys. Rev.* B **72** 205114

[70] Damascelli A, Lu D H and Shen Z-X 2001 From Mott insulator to overdoped superconductor: evolution of the electronic structure of cuprates studied by ARPES *J. Electron Spectrosc. Relat. Phenom.* **117–118** 165–87

[71] Kaminski A *et al* 2004 Identifying the background signal in angle-resolved photoemission spectra of high-tempertature cuprate superconductors *Phys. Rev.* B **69** 212509

[72] Yang K *et al* 2006 Normal state electronic structure in the heavily overdoped regime of $Bi_{1.74}Pb_{0.38}Sr_{1.88}CuO_{6+\delta}$ single-layer cuprate superconductors *Phys. Rev.* B **73** 144507

[73] Kaminski A *et al* 2005 Momentum anisotropy of the scattering rate in cuprate superconductors *Phys. Rev.* B **71** 014517

[74] Zhou X J *et al* 2004 Dichotomy between nodal and antinodal quasiparticles in underdoped $(La_{2-x}Sr_x)CuO_4$ superconductors *Phys. Rev. Lett.* **92** 187001

[75] Sahrakorpi S, Lindroos M, Markiewicz R S and Bansil A 2005 Evolution of midgap states and residual three dimensionality in $La_{2-x}Sr_xCuO_4$ *Phys. Rev. Lett.* **95** 157601

[76] Bansil A, Lindroos M, Sahrakorpi S and Markiewicz R S 2005 Influence of the third dimension of quasi-two-dimensional cuprate superconductors on angle-resolved photoemission spectra *Phys. Rev.* B **71** 012503

[77] Mackenzie A P, Julian S R, Diver A J, McMullan G J, Ray M P, Lonzarich G G, Maeno Y, Nishizaki S and Fujita T 1996 Quantum oscillations in the layered perovskite superconductor Sr_2RuO_4 *Phys. Rev. Lett.* **76** 3786–9

[78] Bergemann C, Julian S R, Mackenzie A P, NishiZaki S and Maeno Y 2000 Detailed topography of the Fermi surface of Sr_2RuO_4 *Phys. Rev. Lett.* **84** 2662–5

[79] Damascelli A *et al* 2000 Fermi surface, surface states and surface reconstruction in Sr_2RuO_4 *Phys. Rev. Lett.* **85** 5194–7

[80] Liebsch A 2001 Fermi surface, surface states and surface reconstruction in Sr_2RuO_4 *Phys. Rev. Lett.* **87** 239701

[81] Damascelli A, Shen K M, Lu D H and Shen Z-X 2001 Fermi surface, surface states and surface reconstruction in Sr_2RuO_4 *Phys. Rev. Lett.* **87** 239702

[82] Shen K M *et al* 2001 Surface electronic structure of Sr_2RuO_4 *Phys. Rev.* B (*Rapid Commun.*) **64** 180502 (R)

[83] Abdel-Jawad M, Kennett M P, Balicas L, Carrington A, Mackenzie A P, McKenzie R H and Hussey N E 2006 Anisotropic scattering and anomalous transport in a high temperature superconductor *Nat. Phys.* **2** 821

[84] Slezak J A and Davis J C 2006 *APS March Meeting 2006, Invited Talk within the Focused Session 'The Electronic Properties of Overdoped Cuprates: The Clean Gateway to High-T_c Superconductivity'*

[85] Hoffman J E, McElroy K, Lee D-H, Lang K M, Eisaki H, Uchida S and Davis J C 2002 Imaging quasiparticle interference in $Bi_2Sr_2CaCu_2O_{8+\delta}$ *Science* **297** 1148–51

[86] Gedik N, Langner M, Orenstein J, Ono S, Abe Y and Ando Y 2005 Abrupt transition in quasiparticle dynamics at optimal doping in a cuprate superconductor system *Phys. Rev. Lett.* **95** 117005

[87] Carbone F *et al* 2006 Doping dependence of the redistribution of optical spectral weight in $Bi_2Sr_2CaCu_2O_{8+\delta}$ *Phys. Rev.* B **74** 064510

[88] Ma Y C and Wang N L 2006 Infrared scattering rate of overdoped $Tl_2Ba_2CuO_{6+\delta}$ *Phys. Rev.* B **73** 144503

[89] Abrahams E and Varma C M 2000 What angle-resolved photemission experiments tell about the microscopic theory for high-temperature superconductors *Proc. Natl Acad. Sci. USA* **97** 5714–16

[90] Zhu L, Hirschfeld P J and Scalapino D J 2004 Elastic forward scattering in the cuprate superconducting state *Phys. Rev.* B **70** 214503

[91] Wakabayashi K, Rice T M and Sigrist M 2005 Enhanced coherence of antinodal quasiparticles in a dirty d-wave superconductor *Phys. Rev.* B **72** 214517

[92] Vojta M, Zhang Y and Sachdev S 2000 Quantum phase transitions in d-wave superconductors *Phys. Rev. Lett.* **85** 4940–3

[93] Kopp A, Ghosal A and Chakravarty S 2006 Competing ferromagnetism in high temperature copper oxide superconductors *Preprint* cond-mat/0606431